Title
Hierarchical Bayesian method for mapping biogeochemical hot spots using induced polarization imaging

Journal
Water Resources Research, 52(1)

ISSN
0043-1397

Authors
Wainwright, Haruko M
Orozco, Adrian Flores
Bücker, Matthias
et al.

Publication Date
2016

DOI
10.1002/2015wr017763

Peer reviewed

AGU PUBLICATIONS

Water Resources Research

RESEARCH ARTICLE

10.1002/2015WR017763

Hierarchical Bayesian method for mapping biogeochemical hot spots using induced polarization imaging

Haruko M. Wainwright[1], Adrian Flores Orozco[2], Matthias Bücker[2,3], Baptiste Dafflon[1], Jinsong Chen[1], Susan S. Hubbard[1], and Kenneth H. Williams[1]

[1]Earth Sciences Division, Lawrence Berkeley National Laboratory, Berkeley, California, USA, [2]Department of Geodesy and Geoinformation, Vienna University of Technology, Vienna, Austria, [3]Steinmann Institute, Department of Geophysics, University of Bonn, Bonn, Germany

Key Points:
- Naturally reduced zones (NRZs) are considered to be biogeochemical hot spots under floodplains
- We developed a noninvasive probabilistic mapping method of NRZs using induced polarization imaging
- This method provides a minimally invasive means to parameterize a floodplain biogeochemical model

Correspondence to:
H. M. Wainwright,
hmwainwright@lbl.gov

Citation:
Wainwright, H. M., A. Flores Orozco, M. Bücker, B. Dafflon, J. Chen, S. S. Hubbard, and K. H. Williams (2016), Hierarchical Bayesian method for mapping biogeochemical hot spots using induced polarization imaging, *Water Resour. Res.*, *52*, 533–551, doi:10.1002/2015WR017763.

Received 1 JUL 2015
Accepted 27 DEC 2015
Accepted article online 30 DEC 2015
Published online 29 JAN 2016

Abstract In floodplain environments, a naturally reduced zone (NRZ) is considered to be a common biogeochemical hot spot, having distinct microbial and geochemical characteristics. Although important for understanding their role in mediating floodplain biogeochemical processes, mapping the subsurface distribution of NRZs over the dimensions of a floodplain is challenging, as conventional wellbore data are typically spatially limited and the distribution of NRZs is heterogeneous. In this study, we present an innovative methodology for the probabilistic mapping of NRZs within a three-dimensional (3-D) subsurface domain using induced polarization imaging, which is a noninvasive geophysical technique. Measurements consist of surface geophysical surveys and drilling-recovered sediments at the U.S. Department of Energy field site near Rifle, CO (USA). Inversion of surface time domain-induced polarization (TDIP) data yielded 3-D images of the complex electrical resistivity, in terms of magnitude and phase, which are associated with mineral precipitation and other lithological properties. By extracting the TDIP data values colocated with wellbore lithological logs, we found that the NRZs have a different distribution of resistivity and polarization from the other aquifer sediments. To estimate the spatial distribution of NRZs, we developed a Bayesian hierarchical model to integrate the geophysical and wellbore data. In addition, the resistivity images were used to estimate hydrostratigraphic interfaces under the floodplain. Validation results showed that the integration of electrical imaging and wellbore data using a Bayesian hierarchical model was capable of mapping spatially heterogeneous interfaces and NRZ distributions thereby providing a minimally invasive means to parameterize a hydrobiogeochemical model of the floodplain.

1. Introduction

Terrestrial biogeochemical processes represent a significant uncertainty in our understanding of carbon and nutrient cycling [e.g., *Heimann and Reichstein*, 2009]. Recent studies have described how small zones in an environment can display enhanced biogeochemical reaction rates and/or fluxes relative to surrounding regions. Compared to contributions from neighboring regions, these biogeochemical hot spots can have a disproportionally large impact on larger-scale biogeochemical cycling [*McClain et al*., 2002; *Vidon et al*., 2010]. *Duncan et al*. [2013], for example, estimated that riparian-zone hollows (lower topographic regions) accounted for more than 99% of total denitrification in a catchment (37 ha), even though the hollows represent only 0.5%–1.0% of the total catchment area. Several other papers have described hot spots associated with regions where groundwater flow upwells or meets organic-rich sediments [*Hedin et al*., 1998; *Hill et al*., 2000]. Other hot spots include wetlands [*Johnston et al*., 2001], hyporheric zones [*Triska et al*., 1984; *Holmes et al*., 1996], and vernal pools [*Capps et al*., 2014].

Identifying and mapping hot spots in sufficient resolution, yet over spatial scales needed to inform modeling, is challenging [*Vidon et al*., 2010]. *Duncan et al*. [2013] used a topographic wetness index (based on a digital elevation map from airborne LiDAR) to estimate the distribution of hot spots of intense denitrification (i.e., riparian-zone hollows). However, *Anderson et al*. [2015] estimated—using the same index—that drier upland soils would contribute to a larger portion of whole-catchment denitrification. Such discrepancy could be attributed to the fact that the subsurface terms (soil thickness and hydraulic conductivity) are often ignored or approximated in the topographic wetness index. Although the topography and other surface indicators (e.g., slope) are often strongly correlated with subsurface biological processes, other factors

(e.g., geology, soil type) may also play a critical role in subsurface biogeochemistry. However, direct measurements of subsurface properties have been mostly limited to drilling wells and sampling cores, which are often invasive and sparse, failing to identify the exact extent of the hot spots or associated controls.

Recently, *Campbell et al*. [2012] and *Qafoku et al*. [2014] reported the presence of naturally reduced zones (NRZs) within aquifer sediments at a former uranium mill-processing site near Rifle, Colorado (USA). This site is located on a floodplain adjacent to the Colorado River. The two studies found that NRZ sediments had elevated concentrations of uranium, organic matter, and geochemically reduced mineral phases, such as metal sulfides, and were often associated with predominantly fine-grained sediment textures. The historical monitoring of pore water chemistry also showed that the elevated concentrations were fairly persistent over time [*Zachara et al*., 2013]. The conceptual model of NRZ formation is that roots, twigs, and other plant materials accumulated during the river depositional process, became buried, and formed the reduced sediments. In addition to these two studies, *Mouser et al*. [2014] found unique microbial characteristics within the NRZs, such as the abundance of iron-reducing Geobacteraceae communities. Recent modeling studies suggested that NRZs have a significant impact on subsurface carbon flux to the atmosphere as well as to the river [*Arora et al*., 2015a, 2015b]. NRZs can therefore be considered the biogeochemical "hot spots" of the Rifle floodplain, having distinct microbial, mineralogical, and geochemical properties.

Floodplain-based NRZs could potentially play an important role in global carbon cycling. Although the floodplains cover a small portion of the Earth's surface, overbank sedimentation at river floodplains is considered to be a significant terrestrial sink of carbon [*Walling et al*., 2006; *Battin et al*., 2009; *Aufdenkampe et al*., 2011]. Floodplains also constantly exchange water, sediment, and geochemical constituents with rivers [*Neff and Asner*, 2001; *Grimm et al*., 2003; *Gomez et al*., 2012]. Subsurface carbon respiration and surface water-groundwater exchanges within floodplains contribute significantly to dissolved organic carbon concentrations and CO_2 outgassing in streams and rivers [*Schindler and Krabbenhoft*, 1998; *Cole et al*., 2007; *Battin et al*., 2008; *Melack*, 2011]. To develop a model describing the coupled hydrologic and biogeochemical behavior of floodplains, we must include the presence and distribution of such hot spots within the subsurface. Unfortunately, conventional borehole data (e.g., sediment properties, solid and aqueous phase geochemistry, microbial community composition) are often spatiotemporally sparse and thus insufficient for resolving subsurface heterogeneity within floodplain deposits [e.g., *Scheibe and Freyberg*, 1995; *Kowalsky et al*., 2011; *Yabusaki et al*., 2011].

Various geophysical methods have been developed in the past several decades to characterize heterogeneous subsurface environments in a noninvasive manner [e.g., *Rubin and Hubbard*, 2005; *Vereecken et al*., 2006; *Hubbard and Linde*, 2011; *Binley et al*., 2015]. Surface electrical methods—based on injecting an electrical current through one pair of electrodes on the ground surface and measuring the electrical potential between a second pair of electrodes—are amongst the most commonly used near-surface geophysical techniques. The geometrical distribution of electrical resistivity from such measurements has been used to delineate geological units, water saturation, and lithological properties [e.g., *Bowling et al*., 2005; *Binley and Kemna*, 2005; *Doetsch et al*., 2012; *Kennedy et al*., 2013]. Particularly, electrical resistivity tomography (ERT) employs tens of electrodes along the profile and measures the electrical potential between them. Tomographic data are then converted to depth-discrete electrical resistivity values along the profile using suitable inversion schemes [e.g., *Binley and Kemna*, 2005]. Electrical resistivity (the inverse of electrical conductivity) is a bulk property of subsurface material associated with its tendency to resist electrical current flow, and has long been known to be correlated with water saturation, pore water chemistry and lithological properties [e.g., *Archie*, 1942].

Recently, the induced polarization (IP) imaging technique—also referred to as complex conductivity or complex resistivity imaging—has been increasingly used to provide additional information on subsurface conditions. Induced polarization phenomena are of electrochemical origin, depending mainly on the presence of metallic minerals and the pore structure. In the presence of metallic minerals, the change in the electrical conduction mechanisms from electrolytic (in the groundwater) to electronic (in the metallic minerals) results in strong polarization effects [e.g., *Pelton et al*., 1978]. Previous studies have reported a linear correlation between the size of metallic minerals and the IP effect [*Wong*, 1979]. In case of porous media without metallic minerals, the polarization effect is primarily controlled by the total mineral-fluid surface area within the sample, which can be estimated from the total mineral surface area per unit pore volume [e.g., *Weller and Slater*, 2015]. As grain size and surface are inversely related, other workers have found a near-inverse

linear relation between the IP effect and effective grain [e.g., *Titov et al*., 2004] and pore size [e.g., *Binley et al*., 2005].

The IP method was initially used in the prospecting for metallic and certain sulfide ores [e.g., *Pelton et al*., 1978] based upon strong polarization enhanced in the presence of metallic and semiconductive minerals [*Wong*, 1979]. More recently, polarization mechanisms occurring in geological materials without metallic admixtures, such as membrane polarization [e.g., *Marshall and Madden*, 1959; *Bücker and Hördt*, 2013] or the polarization of the Stern layer [e.g., *Revil and Florsch*, 2010], have been found to be sensitive to different hydrogeological (texture, grain/pre size, saturation, etc.) and geochemical (e.g., salinity, pH) parameters. Particularly, the membrane polarization model has been proposed for rocks with a dispersed clay fraction [e.g., *Marshall and Madden*, 1959], based on the theory that clay minerals coating the quartz grains or located in pore-throats produce local concentration gradients under applied external voltage [*Titov et al*., 2002; *Scott and Barker*, 2003]. In addition, the IP measurements have recently been used to detect and map subsurface (bio)geochemical properties associated with microbe-induced mineral precipitation [e.g., *Ntarlagiannis et al*., 2005; *Williams et al*., 2009; *Flores Orozco et al*., 2011; *Chen et al*., 2013; *Abdel Aal et al*., 2014].

Ground-based tomographic IP measurements are typically acquired using a similar electrode configuration as ERT. In addition to the resistivity measurements, the time decay of the electric potential is measured after the current injection is stopped. Recently, multielectrode IP surveys (commonly referred to as tomographic surveys), in combination with appropriate inversion techniques, have enabled the high spatial resolution imaging of the complex electrical resistivity in the subsurface [*Binley and Kemna*, 2005].

Previous studies at the Rifle site reported the application of the IP method for monitoring subsurface microbial processes stimulated through organic carbon addition [*Williams et al*., 2009]. These field studies revealed that the IP method is suitable for detecting an increase in the polarization effect accompanying the precipitation of iron sulfides (e.g., FeS) and changes in the chemical composition of groundwater, particularly the concentration of electroactive ions, such as Fe (II) [*Flores Orozco et al*., 2011; *Chen et al*., 2013]. A recent study demonstrated that the polarization response in geochemically reduced, biostimulated sediments remained much higher than for background aquifer materials (i.e., those unimpacted by carbon addition) at the Rifle site over the broad frequency bandwidth (0.06–120 Hz) used for the IP measurements [*Flores Orozco et al*., 2013]. Given the natural enrichment in conductive and semiconductive metal sulfides in NRZ sediments relative to non-NRZ sediments [*Campbell et al*., 2012; *Qafoku et al*., 2014], surface IP methods are well suited for the noninvasive delineation of NRZs within aquifer sediments.

As with other geophysical methods, interpretation of IP imaging results in terms of biogeochemical properties is hindered by uncertainties and often site-specific relationships between the electrical parameters (in this case, the magnitude and phase shift of the complex electrical resistivity) and mineralogical-geochemical properties. Other mechanisms exist that can engender a measurable polarization response in the subsurface, which also complicates interpretation of IP data. In particular, the mixture of materials with different textural properties (e.g., grain size) is related to an increase in the polarization effect due to membrane polarization mechanisms [e.g., *Revil and Florsch*, 2010; *Bücker and Hördt*, 2013]. Hence, IP measurements collected over the full extent of a floodplain might be sensitive to subsurface properties not solely limited to the presence of reduced sediments within NRZ's, but also due to lithological boundaries and corresponding changes in mineralogical and textural properties [e.g., *Börner et al*., 1996; *Slater et al*., 2014].

Bayesian methods offer an approach to integrate geophysical data sets and point measurements, including their uncertainty, in a consistent manner [e.g., *Hubbard et al*., 2001; *Chen et al*. 2004, 2006; *Sassen et al*., 2012; *Wainwright et al*., 2014]. In particular, reactive facies or zonation approaches have recently been developed within the Bayesian framework to identify regions that have unique distribution of physical and geochemical properties using geophysical data [*Chen et al*., 2006; *Sassen et al*., 2012; *Wainwright et al*., 2014]. Instead of estimating hydrological or biogeochemical properties directly, the zonation approaches aim to delineate zones and their associated property distributions. These methods take advantage of the often-coupled nature of physical, microbiological, and geochemical properties of subsurface materials and the sensitivity of geophysical responses to at least one of the properties to identify and characterize reactive facies or zones.

In this study, we extend the zonation concept to estimate the distribution of NRZs in a three-dimensional (3-D) domain over the Rifle floodplain using surface time domain-induced polarization (TDIP) measurements.

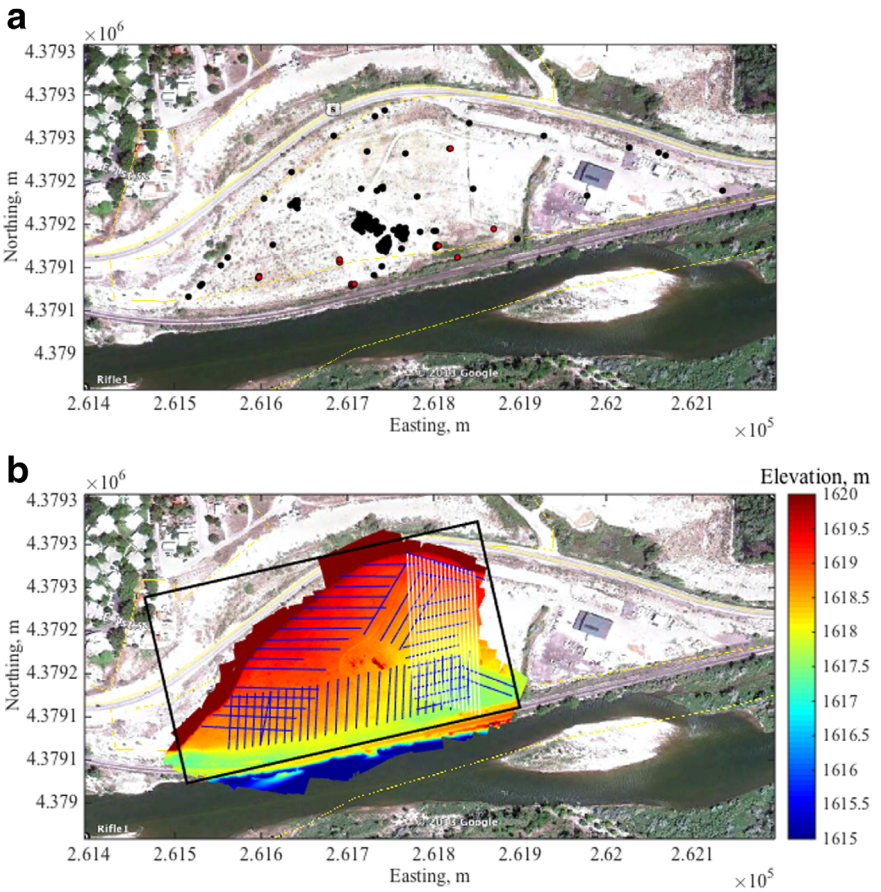

Figure 1. (a) Rifle floodplain with well locations, and (b) digital elevation model (in meter) with ERT lines (white region) and TDIP lines (blue lines). In Figure 1a, the black circles are the well locations constructed prior to 2013, and the red circles represent the wells that were drilled in 2014. The site picture is obtained from Google Earth. The Colorado River bounds the south of the site. In Figure 1b, the black rectangle represents the domain used for the estimation and reactive transport modeling.

The distribution of the complex electrical resistivity properties of the subsurface was obtained after the inversion of the TDIP data. We developed a Bayesian approach to integrate wellbore lithological data and IP inversion results, and estimated the distribution of NRZs in a probabilistic manner. In order to develop a high-resolution 3-D representation of the subsurface, we used a digital elevation model (DEM) inferred from an aerial landscape imaging survey and structure-from-motion techniques. We estimated hydrostratigraphic interfaces using electrical resistivity images from both the IP data sets and electrical resistivity tomography (ERT) data available at the site. Such hydrostratigraphic interfaces are important for hydrological and geochemical modeling at this site, as they control vertical infiltration and lateral groundwater flow. To the authors' knowledge, this is the first study to apply the IP method for delineating such biogeochemical hot spots in a probabilistic manner and to establish a methodology for integrating multiple spatially extensive above ground and below ground data sets capable of informing biogeochemical models at the floodplain scale.

2. Site Information and Data

2.1. Site Description

The Rifle site (Figure 1) is located on a floodplain adjacent to the Colorado River in northwestern Colorado [e.g., *Williams et al.*, 2009]. The site was formerly used as a vanadium and uranium ore processing facility, which caused soil and groundwater contamination by uranium and other heavy metals. The site is currently a part of the U.S. Department of Energy's (DOE) Uranium Mill Tailings Remedial Action program, which includes long-term monitoring activities following excavation and removal of mill tailings and tailings-contaminated surface materials. The Rifle site currently serves as a community field laboratory for research in

biogeochemical characterization, bioremediation, subsurface microbial characterization, and nutrient cycling [e.g., *Williams et al*., 2011; *Yabusaki et al*., 2011; *Castelle et al*., 2013; *Wrighton et al*., 2014].

The site hydrostratigraphy consists of three principal units, referred to hereafter from surface to base of the aquifer as: the fill layer, the Rifle Formation, and the Wasatch Formation. The fill layer—comprised of silt-rich loess deposits derived from a quarry abutting the site to the northeast—was artificially constructed to cover the ground surface postreclamation and also to reduce the amount of infiltration reaching the groundwater. The fill thickness is ~1–3 m over the area, although it is thicker in areas where a greater depth of contaminated soil was excavated due to higher contamination levels. A shallow unconfined aquifer, the Rifle Formation, is comprised of alluvium deposited by the Colorado River that includes unconsolidated clays, silts, sands, gravels, and cobbles (DOE, 1999). Primarily composed of weathered clayey siltstone, the low-permeability Wasatch Formation underlies the Rifle Formation at depths of 5–8 m below ground surface and serves as a local aquitard to the saturated alluvium at the site. Additionally, the Wasatch Formation includes discontinuous sandstone lenses, a small fraction of which contain visible pyrite grains, with such materials observed both within drilling-recovered materials and in outcrops adjoining the site.

2.2. Core Data and Lithological Logs

This site has 171 wells with well-documented lithological logs constructed over more than 20 years (in Figure 1a, the black circles are the well locations constructed prior to 2013). Sixteen new wells were added in 2014 for additional geochemical characterization (red circles in Figure 1a). Through extensive geochemical and microbiological analysis of Rifle core data, several studies [*Campbell et al*., 2012; *Qafoku et al*., 2014; *Janot et al*., 2015] identified and characterized two NRZ localities at the site (spatially separated by ~65 m). To identify NRZ locations along each well, we relied on the lithological log constructed for each of those wells. These log reports have a standard format and include the description of core texture, color (using Munsell soil color chart), and other features. They also provide the interface depths of the fill, Rifle Formation, and Wasatch Formation. Those reports are archived, quality controlled, and made publically available by DOE at URL http://gems.lm.doe.gov/#site=RFO. By comparing the well log reports and the sample locations in *Campbell et al*. [2012] and *Qafoku et al*. [2014], we found that the sediment description of "dark color" or "reduced" provided an excellent match to the NRZ locations.

2.3. Surface Elevation Data

A high-resolution surface elevation map was provided by a kite-based aerial system, which lifts a consumer-grade digital camera (Sony Nex-5R) about 40 m above the ground surface [*Smith et al*., 2009]. The reconstruction procedure was performed using a commercial computer vision software package (PhotoScan from Agisoft LLC). The reconstruction involved automatic image feature detection/matching, structure-from-motion and multiview-stereo techniques for 3-D point-cloud generation, and georeferenced mosaic reconstruction. High-accuracy georeferencing was enabled by using a network of ground control points surveyed with a high-precision centimeter-grade RTK DGPS system.

A digital terrain model was inferred from the digital surface model by using a moving average filter to remove sharp positive variations, which is adequate for this site because of the sparse and low vegetation and the relatively smooth changes in terrain elevation. The comparison to the ground surface elevation at wells surveyed with high-precision GPS showed excellent agreement. The digital elevation model was used to convert the depth information of the ERT and IP data to the elevation after the inversion. Since elevation variability is low along each line (<1.5 m), no formal treatment of elevation effects on data inversion was undertaken.

2.4. Geophysical Data Acquisition and Inversion

The ERT data set was acquired on the eastern side of the site along 17 parallel profiles (white lines in Figure 1b), each one being 166.5 m long and 5 m distant from the adjacent profile. Resistance measurements were collected using the MPT-DAS-1 system with 112 stainless steel electrodes having an electrode separation of 1.5 m and using a dipole-dipole configuration involving dipole lengths ranging from 1.5 to 18 m with the distance between the closest injection and potential electrodes equal to or smaller than 3 times the dipole length. The survey configuration was chosen to obtain a high signal-to-noise ratio and to image both near-surface features and the deeper Rifle-Wasatch interface. Ten percent of measurements were collected in a normal and reciprocal mode to evaluate data quality.

The IP data set was collected using a time domain-induced polarization (TDIP) method along 65 profiles of various lengths over the floodplain (Figure 1b). In the TDIP method, the transient decay of voltage is measured after current shut-off, typically in the form of an integral of decay curves over a predefined time-window (so-called integral chargeability). TDIP measurements at the site were collected using the Syscal Iris Pro Switch equipment with a square-wave current injection, 50% duty cycle, and a pulse length of 2 s. The integral chargeability measurements were carried out using 20 windows during voltage decay between 240 and 1840 ms after current shut-off. Tomographic measurements were collected by deploying stainless steel electrodes with an electrode separation of 1.8 m and using a dipole-dipole "skip-2" and "skip-3" measuring protocol (i.e., for a dipoles length of 5.4 and 7.2 m, respectively). The sequence of dipole-dipole measurements was carefully arranged to (1) minimize unwanted electromagnetic coupling effects in the data, avoiding potential measurements with electrodes located inside the current dipole (as suggested in *Pelton et al*. [1978] and *Flores Orozco et al*. [2013]), (2) prevent voltage measurements using electrodes, which might be polarized due to previous current injection [*LaBrecque and Daily*, 2008; *Williams et al*., 2009], and (3) increase the signal-to-noise ratio for an intended exploration depth of 8 m, i.e., the bottom of the aquifer [e.g., *Williams et al*., 2011]. All measurements were collected as normal and reciprocal pairs for estimation of the data error. The IP measurements were collected with symmetric arrays (i.e., the measuring equipment placed at the center of the electrode array) with a maximum of 36 electrodes, considering that longer profiles revealed a significant increase in the normal-reciprocal misfit for the measurements of the decay curve, probably due to greater impact of electromagnetic coupling on the data.

Both the ERT and TDIP data sets were inverted in a two-dimensional domain along each transect using CRTomo, which is a smoothness-constraint inversion code based on a finite element algorithm [*Kemna*, 2000]. The resistivity and phase shift values at each pixel were then assigned at the corresponding point within the 3-D floodplain domain (the black rectangle Figure 1b) and used in the 3-D estimation. The TDIP inversion results provided the distribution of the complex resistivity, expressed in terms of its magnitude and phase-shift, while the inversion of ERT data was solved for the magnitude of resistivity. For the inversion of the ERT measurements, data have been cleaned from a very limited number of outliers. In the reciprocal-versus-normal measurements, the measurements with the highest misfit were related to lowest measured voltage. The analysis of the normal-reciprocal misfit was used to estimate the relative error. We removed the measurement with smallest voltage difference ($<$2 mV), representing about 2% variations in the data. For the inversion of TDIP measurements, chargeability values were linearly converted to frequency domain phase values (at the fundamental frequency of 0.125 Hz), by assuming a constant-phase response [*Kemna et al*., 1997]. This approach has been demonstrated to provide consistent results in previous studies [*Slater and Binley*, 2006; *Mwakanyamale et al*., 2012; *Flores Orozco et al*., 2012a, 2012b]. *Flores Orozco et al*. [2012a] also showed that the two existing approaches—frequency domain measurements and converted time domain data sets—did not create a significant difference in the correlation (below 5%) between hydrocarbon concentrations and the magnitude and phase shift of the complex electrical resistivity.

The estimation of the data errors was performed on the analysis of the misfit between normal and reciprocal measurements, following the methodology developed by *Flores Orozco et al*. [2012b]. Prior to the inversion, we removed outliers in the data, which were defined as those measurements associated with large discrepancies between normal and reciprocal phase readings (i.e., the normal-reciprocal misfit of each configuration exceeding 2 times the normal-reciprocal standard deviation of the entire data set). After the inversion, we removed the low-sensitivity area from the 2-D image of the phase shift and resistivity. We used a threshold value in the cumulated sensitivity, which is a measure of how much the entire data set changes due to a changing model value in each cell [*Kemna*, 2000] and has been previously used to assess the variable image resolution [*Kemna*, 2000; *Nguyen et al*., 2009]. As discussed in the study of *Flores Orozco et al*. [2013], the uncertainty in IP imaging results increases with decreasing the cumulated sensitivity.

3. Exploratory Data Analysis of Inverted Geophysical Images

Resistivity images obtained from the inversion of both ERT and TDIP data sets were used to map the depths of the fill-Rifle and Rifle-Wasatch interfaces, since both the fill layer and Wasatch Formation have lower resistivity (owing to higher clay and/or silt contents) than the Rifle Formation. While the dense ERT measurements were located only in the western part of the floodplain, the TDIP measurements covered most of the

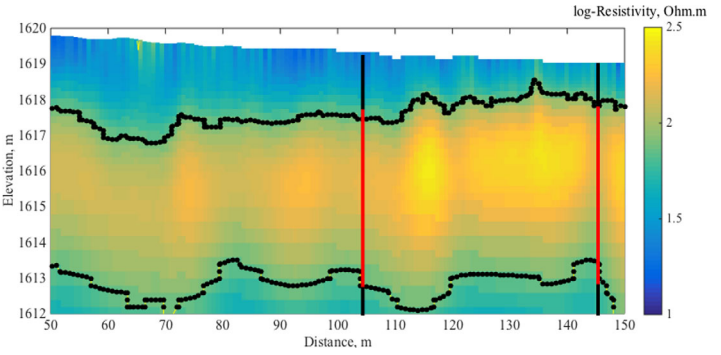

Figure 2. Two-dimensional Resistivity image from the surface ERT (one of 17 lines). The threshold resistivity value (70.0 Ohm m) is marked by the black curves, representing the two interfaces (Fill-Rifle and Rifle-Wasatch). The vertical black lines are the colocated well locations. The red portion represents the Rifle Formation, so that the black-red boundary represents the interface.

floodplain. We delineated the interfaces by setting the threshold resistivity values and correlated them to the depths reported for colocated wells. We determined the threshold values to maximize the correlations between the borehole-determined interface and the geophysically determined one. For ERT, the threshold value was 70.0 Ohm m for both the Wasatch and fill interfaces. For TDIP, 66.1 Ohm m was used for the fill interface. Figure 2 shows the correspondence between the interfaces based on the threshold resistivity values and the ones from the wellbore lithology data in one of the ERT images.

Figures 3a and 3b show the significant correlations between the ERT-derived depths and borehole-derived depths for the fill-Rifle and Rifle-Wasatch interfaces. The correlation coefficients were 0.75 (p-value: 5.3×10^{-2}) for the Rifle-Wasatch interface and 0.85 (p-value: 5.2×10^{-5}) for the fill-Rifle interface, respectively. Since there is a shift (or bias) from the one-to-one line, we performed a linear regression, and used the linearly fitted line for estimating the interface depths. The standard deviation of the linear-fitting residuals was 0.48 m for the Rifle-Wasatch and 0.25 m for the fill-Rifle, respectively. We consider that the scatters resulted from the variability in the lithology and texture of each geologic layer over the floodplain. Similarly, Figure 3c shows a correlation between the TDIP-derived depths and wellbore-derived depths for the fill-Rifle interface (correlation coefficient: 0.83, and p-value: 6.4×10^{-6}). The standard deviation of the linear-fitting residuals was 0.24 m. Although the TDIP has a much larger coverage over the floodplain, we did not use the TDIP data for estimating the Rifle-Wasatch interface, since the TDIP data were focused on the shallower depths within the Rifle Formation, and had limited sensitivity to the Wasatch Formation.

Previous monitoring studies at the Rifle Site demonstrated an increase in the IP phase shift accompanying the precipitation of metallic minerals (e.g., FeS) resulting from stimulated microbial activity [*Williams et al*., 2009; *Flores Orozco et al*., 2011; *Flores Orozco et al*., 2013]. These studies were, however, based on monitoring data sets collected over the same profile, i.e., with no changes in lithology. A diversity of polarization-generating mechanisms can underlie an anomalous IP response, with variations in sediment texture,

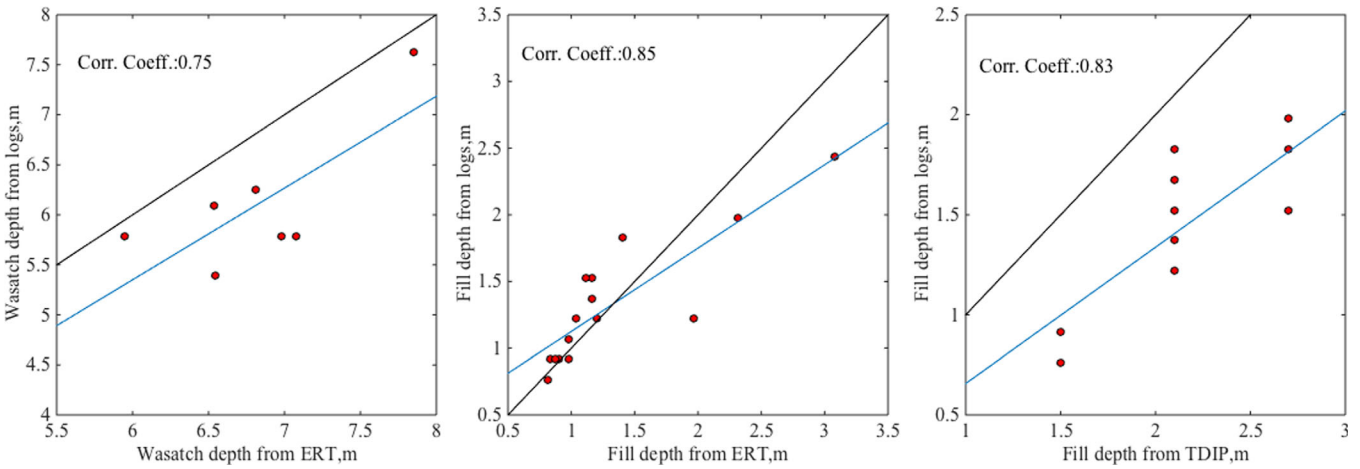

Figure 3. Correlations between (a) ERT-derived and well-derived Wasatch depths, (b) ERT-derived and well-derived Fill depths, and (c) IP-derived and well-derived Fill depths. In Figures 3a–3c, the red dots are data values, the black lines are the one-to-one lines, and the blue lines are the regression-based best fit lines. The correlation coefficient (Corr. Coeff.) is included in each plot.

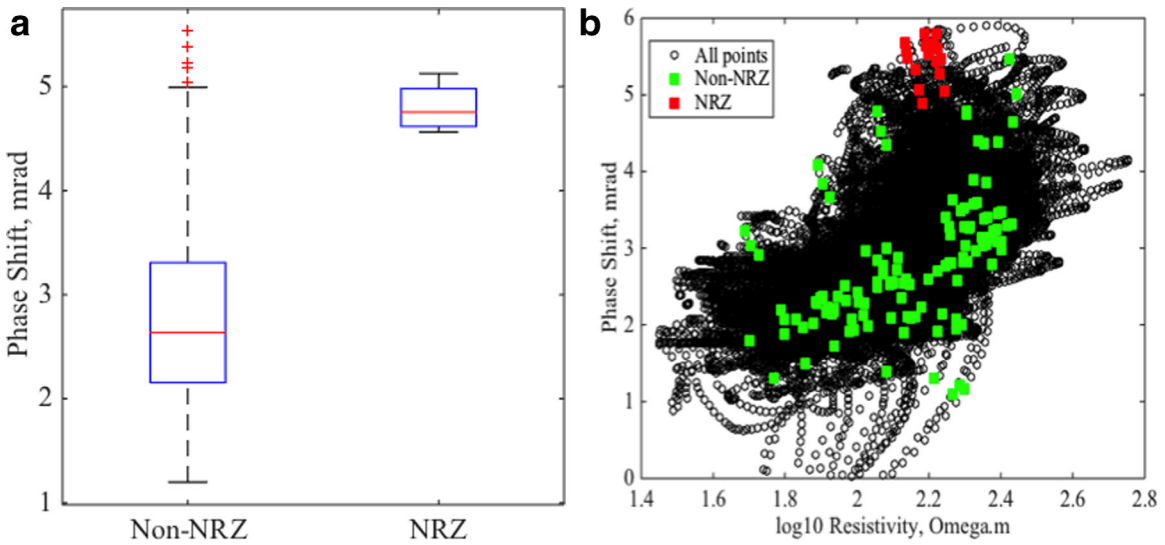

Figure 4. (a) Boxplot to show the phase shift distributions in Non-NRZs and NRZs, and (b) cross-correlation plot for resistivity and phase shift within the Rifle Formation. In Figure 4a, the central red line is the median, the edges of the box are the 25th and 75th percentiles, and the whiskers extend to the 99th percentiles. The red crosses are outliers plotted individually. In Figure 4b, geophysical NRZ and non-NRZ values at wellbore locations are plotted in red and green circles, respectively.

mineralogy, and fluid composition all contributing the polarization/resistivity signature of subsurface materials. Since the current study deals with the change in the electrical responses at a much larger scale (200 × 500 m) than previous studies at the site (30 m), we need to consider the variation in the lithology and other properties of the aquifer.

By comparing the TDIP images and colocated lithological data, we found that NRZs tend to have a higher phase shift, although there are some exceptions (Figure 4a). Plotting the phase shift along with the resistivity at each pixel in Figure 4b shows that the resistivity and phase shift are correlated to each other (the correlation coefficient is 0.72). It is consistent with several studies, in which the higher phase shift is associated with the higher resistivity [*Slater et al*., 2005]. Based on the lithological logs, we identified two clusters in the resistivity-phase shift domain: one for NRZ (the red dots in Figure 4b) and the other for non-NRZ (the green dots in Figure 4b). The distribution of non-NRZ is much broader, possibly because the spatial extent of non-NRZ is much larger, and hence non-NRZs have a larger variability in the resistivity and phase shift associated with lithological properties. Taking into account these two clusters, we used both resistivity and phase shift data simultaneously to identify the NRZ locations and defined the NRZ response in the resistivity-phase shift space as bivariate distributions.

In addition, we observed that a small subset of the TDIP profiles revealed the highest phase-shift values within the Wasatch rather than the Rifle Formation. For example, the inversion results at two lines (in Figure 5) show that a clear IP anomaly associated with an NRZ (confirmed by the colocated wells; Figure 5a) and one line associated with high polarization effects in the Wasatch Formation (Figure 5b). These deeper anomalies were inferred to result from pyrite-bearing sandstone lenses reported in lithological data from colocated drilling locations. Plots in Figure 5 reveal that if the increased phase-shift is associated with an NRZ, the highest phase shift is located in the aquifer materials (Figure 5a). The high polarization due to metallic minerals in the Wasatch (but not NRZ) leads to the creation of artifacts with high phase shift values in the aquifer zone (Figure 5b). Their unintentionally shallow depth in the imaging results is thought to be an artifact resulting from the smoothness constraint used in the inversion.

To remove such artifacts, we considered polarizable anomalies as NRZs only when the highest phase-shift value was located within the Rifle Formation. Although different approaches have been suggested to solve for sharp contrasts in the inversion and improve the resolution of the electrical images [e.g., *Blaschek et al*., 2008; *Caterina et al*., 2014], such strategies require sufficient information about the geometry and characteristics of the interfaces to avoid the creation of further artifacts. Considering that it is not possible to know a priori the existence and geometry of NRZ locations, we believe that the smoothness inversion is an adequate approach to validate the application of the IP imaging method to characterize NRZs.

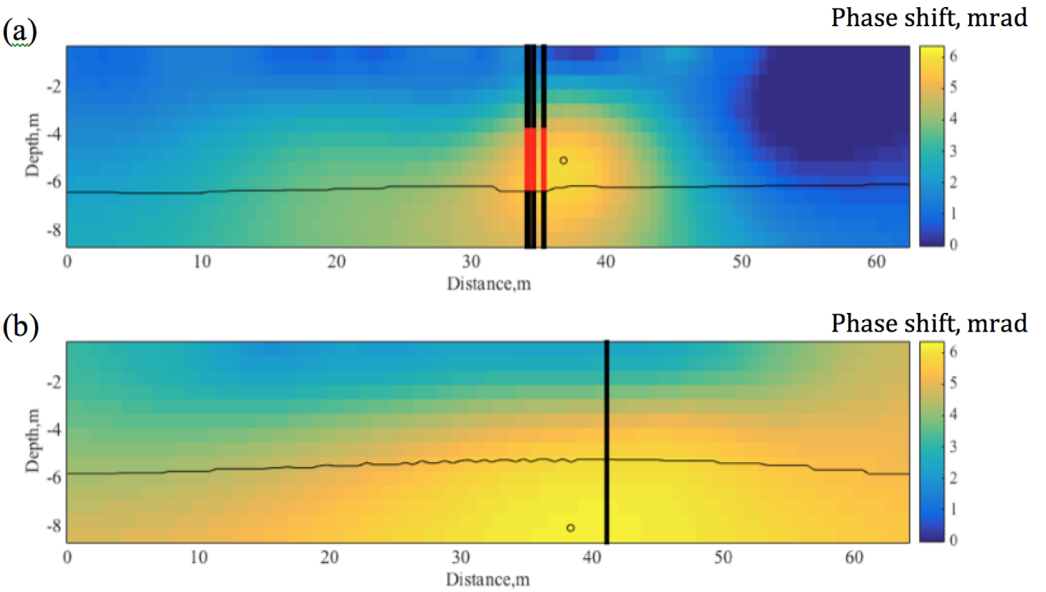

Figure 5. Two-dimensional cross section of the inverted phase shift (mrad) from the TDIP data at (a) the line that had a confirmed NRZ within the Rifle Formation, and at (b) the line that had a confirmed pyrite lens in the Wasatch Formation. The small circle in each figure is the highest phase shift in the domain, and the thin black line is the estimated Rifle-Wasatch interface. The thick black vertical lines indicate colocated well locations. The red lines in Figure 5a are the confirmed NRZs.

4. Statistical Method

Bayesian hierarchical models have been used in the past to integrate multitype and multiscale data sets in a consistent manner, as well as to integrate complex processes [e.g., *Wikle et al*., 2001; *Wainwright et al*., 2014; *Hermans et al*., 2015]. The goal of this estimation is to determine the posterior distribution of heterogeneous properties (or property fields) conditioned on all the given data sets and data model parameters $\boldsymbol{\alpha}$, $p(field|data, \boldsymbol{\alpha})$. In a Bayesian hierarchical model, the posterior distribution can be divided into three statistical submodels represented by conditional distributions: (1) a data model, $p(data|field, \boldsymbol{\alpha})$, which represents the data as a function of the property field and parameters $\boldsymbol{\alpha}$; (2) a process model, $p(field|\boldsymbol{\beta})$, which describes the property field as function of process model parameters $\boldsymbol{\beta}$; and (3) a prior model, $p(\boldsymbol{\alpha},\boldsymbol{\beta})$, which defines the prior information of parameters [*Wikle et al*., 2001]. In the geological environment, one of commonly used process models is often a geostatistical model, which describes a subsurface heterogeneous field as a function of spatial dependence parameters. The hierarchical approach breaks down a complex posterior distribution into a series of simple models, and hence enables us to capture complex relationships easily.

4.1. Interface Estimation

We define each interface as a two-dimensional (2-D) field (e.g., a surface in the 3-D domain). We denote the interface at ith pixel by d_i, where $i = 1, \ldots, n$. The goal is to estimate the posterior distribution $p(\{d_i\}|\boldsymbol{z}_{ERT}, \boldsymbol{z}_{IP}, \boldsymbol{z}_L)$ of the interface field $\{d_i\}$ (i.e., the interface at all the pixels), conditioned on the ERT data (resistivity) $\boldsymbol{z}_{ERT}$, the IP data $\boldsymbol{z}_{IP}$, and well log data $\boldsymbol{z}_L$. By applying the Bayes' rule under the assumption that $\boldsymbol{z}_{ERT}$, $\boldsymbol{z}_{IP}$, and $\boldsymbol{z}_L$ are conditionally independent given the interface locations $\{d_i\}$, we can write the posterior distribution of the interface field as $p(\{d_i\}|\boldsymbol{z}_{ERT}, \boldsymbol{z}_{IP}, \boldsymbol{z}_L) \propto p(\boldsymbol{z}_{ERT}|\{d_i|i \in C_{ERT}\})\, p(\boldsymbol{z}_{IP}|\{d_i|i \in C_{IP}\})\, p(\{d_i\}|\boldsymbol{z}_L)$, where C_{ERT} and C_{IP} are indices of pixels that are colocated either with ERT or IP data, respectively.

The first two conditional distributions $p(\boldsymbol{z}_{ERT}|\{d_i|i \in C_{ERT}\})$ and $p(\boldsymbol{z}_{IP}|\{d_i|i \in C_{IP}\})$ represent the data model, specifically the dependence of the interface depth on data value at each pixel. At the geophysical data locations ($i \in C_{ERT}$ and $i \in C_{IP}$), we assume that the data values can be described by $z_{ERT,i} = a_1 d_i + a_2 + \varepsilon_{ERT}$ and $z_{IP,i} = b_1 d_i + b_2 + \varepsilon_{IP}$, where ε_{ERT} and ε_{IP} are the error terms associated with the uncertainty and/or variability of the correlations between the interface depths and ERT/IP imaging results (Figures 3a–3c), and a_l and b_l ($l = 1, 2$) are the linear-fitting terms to fix the bias from the one-to-one line in Figures 3a–3c. We also assume that ε_{ERT} and ε_{IP} follow the independent normal distribution with zero-mean and the variance σ_{ERT} and σ_{IP}, determined from the correlation plots (Figures 3a–3c).

Furthermore, we assume that $\{d_i\}$ is a multivariate Gaussian random field described by geostatistical parameters, we can derive an analytical form of this posterior distribution as a multivariate normal distribution with mean $Q^{-1}\boldsymbol{g}$ and variance Q^{-1}, where $Q = {\Sigma_c}^{-1} + \mathrm{A}_{\mathrm{ERT}}^{\mathrm{T}}\mathrm{D}_{\mathrm{ERT}}^{-1}\mathrm{A}_{\mathrm{ERT}} + \mathrm{A}_{\mathrm{IP}}^{\mathrm{T}}\mathrm{D}_{\mathrm{IP}}^{-1}\mathrm{A}_{\mathrm{IP}}$ and $\boldsymbol{g} = {\Sigma_c}^{-1}\boldsymbol{\mu}_c + \mathrm{A}_{\mathrm{ERT}}^{\mathrm{T}}\mathrm{D}_{\mathrm{ERT}}^{-1}\boldsymbol{z}_{\mathrm{ERT}} + \mathrm{A}_{\mathrm{IP}}^{\mathrm{T}}\mathrm{D}_{\mathrm{IP}}^{-1}\boldsymbol{z}_{\mathrm{IP}}$ (Appendix A). In Q and $\boldsymbol{g}$, $\boldsymbol{\mu}_c$ and Σ_c are the conditional mean and covariance given the point (i.e., well) data and geostatistical parameters. $\mathrm{D}_{\mathrm{ERT}}$ and D_{IP} are the data covariance matrices; each of the diagonal components is σ_{ERT} and σ_{IP}. $\mathrm{A}_{\mathrm{ERT}}$ and A_{IP} are m_{ERT}-by-n and m_{IP}-by-n sparse matrices, where $\mathrm{A}_{\mathrm{ERT},ji} = 1$ if ith pixel has jth data point; otherwise $\mathrm{A}_{\mathrm{ERT},ji}$ is 0. m_{ERT} and m_{IP} are the number of data points of ERT and IP, respectively.

4.2. Natural Reduced Zone Estimation

To map the NRZ locations, we define a indicator random field $\{f_i\}$ in the 3-D domain ($i = 1, \ldots, n_{3D}$) such that

$$f_i = \begin{cases} 1, \text{ if } i\text{th pixel is in NRZs} \\ 0, \text{ otherwise} \end{cases}. \tag{1}$$

We consider the resistivity and phase shift as the data vectors for resistivity ($\boldsymbol{r}$) and phase shift ($\boldsymbol{\phi}$). Each data point has the data values r_i and ϕ_i at a subset of pixels colocated with the IP data locations ($i \in C_{\mathrm{IP,3D}}$). We also define the depth-discrete well log data vector $\boldsymbol{z}_{\mathrm{W,3D}}$, each element of which is either 0 or 1, since they are the direct measurements of indicators.

As a data model, we follow previous studies that defined geophysical data values having distinct distributions, depending on the indicator type [*Chen et al.*, 2004, 2006; *Wainwright et al.*, 2014]. We assume that the resistivity and phase shift in ith pixel (r_i and ϕ_i) follow distinct bivariate distributions, depending on whether ith pixel is in a NRZ ($f_i = 1$) or not ($f_i = 0$). Instead of univariate distributions used in previous studies [*Chen et al.*, 2006; *Wainwright et al.*, 2014], we assume that the bivariate distributions can represent the correlation coefficients found in the data sets (Figure 4b). We have two sets of distributions:

$$\begin{aligned} p(r_i, \phi_i | f_i = 0, \Phi_0) &= \mathrm{BiN}(\boldsymbol{\mu}_0, \Phi_0) \\ p(r_i, \phi_i | f_i = 1, \Phi_1) &= \mathrm{BiN}(\boldsymbol{\mu}_1, \Phi_1) \end{aligned} \tag{2}$$

where BiN represents the bivariate normal distribution with the mean vector $\boldsymbol{\mu}_l$ and the two-by-two covariance matrix Φ_l ($l = 0,1$). The mean vector $\boldsymbol{\mu}_1$, for example, includes the mean resistivity and mean phase shift at the NRZ locations ($f_i = 1$). The covariance matrix is a function of the resistivity variance, phase shift variance, and their correlation coefficient (shown in Figure 4b). We assume that the covariance is uncertain and needs to be estimated, since the variances tend to be underestimated from a limited number of samples. We estimate the covariance matrices Φ_0 and Φ_1 together in the estimation. The data parameter matrix is defined as $\boldsymbol{\alpha} = \{\Phi_0, \Phi_1\}$.

The goal is to estimate the joint posterior distribution of the indicator field $\{f_i\}$ conditioned on the IP data ($\boldsymbol{r}$ and $\boldsymbol{\phi}$) and well log data ($\boldsymbol{z}_{\mathrm{W,3D}}$), which is the marginal distribution of $p(\{f_i\}, \boldsymbol{\alpha}|\boldsymbol{r}, \boldsymbol{\phi}, \boldsymbol{z}_{\mathrm{W,3D}})$. By assuming resistivity and phase pairs are independent given indicator variable, $\{f_i\}$, and using the Bayes rule, we can write this posterior distribution as:

$$\begin{aligned} p\left(\{f_i\}, \boldsymbol{\alpha} | \boldsymbol{r}, \boldsymbol{\phi}, \boldsymbol{z}_{\mathrm{W,3D}}\right) &\propto p\left(\boldsymbol{r}, \boldsymbol{\phi} | \left\{f_i, i \in C_{\mathrm{IP,3D}}\right\}, \boldsymbol{\alpha}\right) p\left(\{f_i\} | \boldsymbol{z}_{\mathrm{W,3D}}\right) p(\boldsymbol{\alpha}), \\ &= \prod_{i \in C_{\mathrm{IP,3D}}} p(r_i, \phi_i | f_i, \boldsymbol{\alpha}) p\left(\{f_i\} | \boldsymbol{z}_{\mathrm{W,3D}}\right) p(\boldsymbol{\alpha}), \\ &= \prod_{i \in C_{\mathrm{IP,3D}}, f_i = 0} p(r_i, \phi_i | f_i = 0, \Phi_0) \prod_{i \in C_{\mathrm{IP,3D}}, f_i = 1} p(r_i, \phi_i | f_i = 1, \Phi_1) \\ &\quad p\left(\{f_i\} | \boldsymbol{z}_{\mathrm{W,3D}}\right) p(\boldsymbol{\alpha}). \end{aligned} \tag{3}$$

The first conditional distribution $p(\boldsymbol{r}, \boldsymbol{\phi}|\{f_i|i \in C_{\mathrm{IP,3D}}\}, \boldsymbol{\alpha})$ is a data model that defines the distribution of the data values given the occurrence of an NRZ or not, which is defined in equation (2). The latter conditional distribution $p(\{f_i\}|\boldsymbol{z}_{\mathrm{W,3D}})$ represents the indicator field given the depth-discrete well log data as conditional points. The prior distribution must be defined for the covariances as $p(\boldsymbol{\alpha})$.

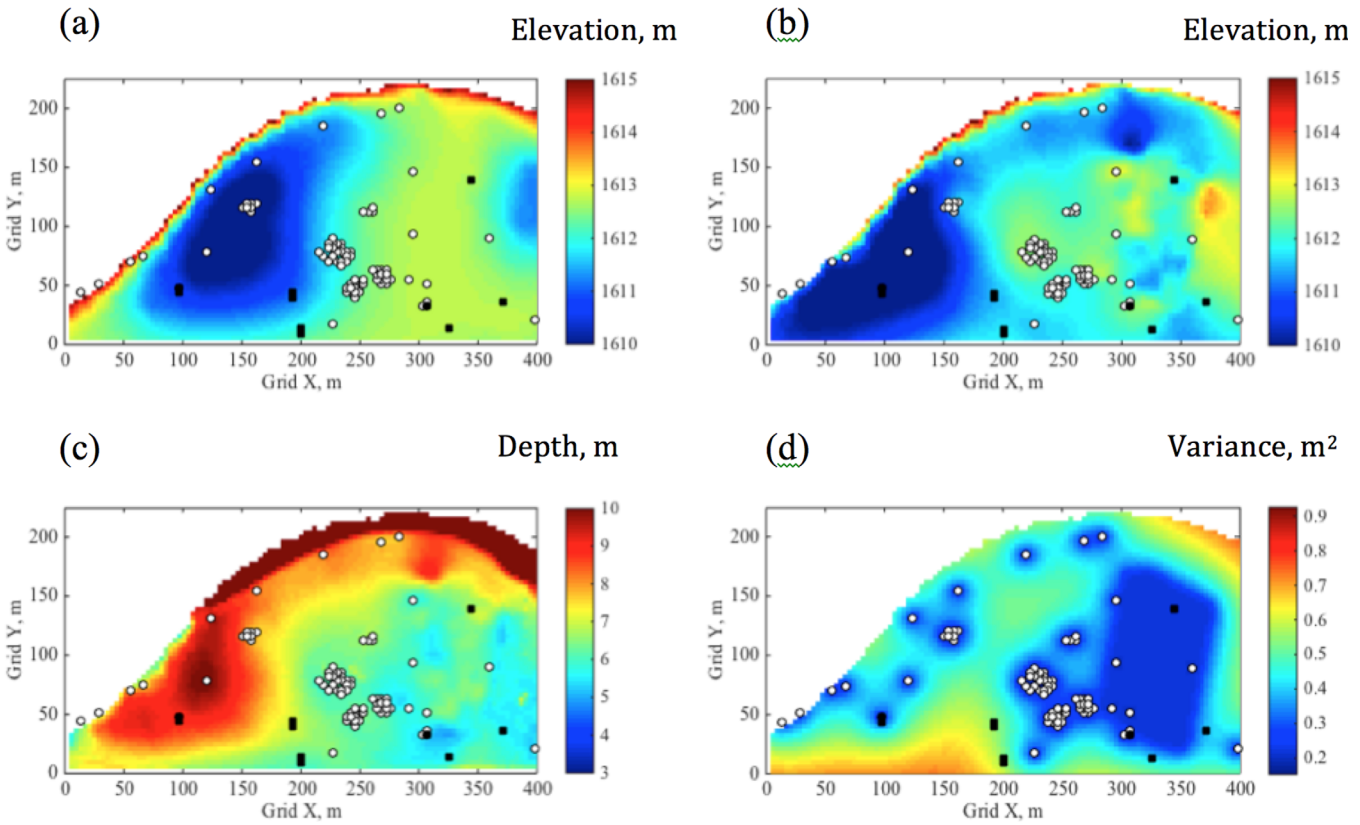

Figure 6. Rifle-Wasatch interface estimation results: (a) the previously estimated elevation in meters, (b) the mean estimate of the elevation in meters, (c) the depth in meters, and (d) the estimation variance in squared meters. The white circles are the well locations used for the estimation, and the black circles are the well locations used for validation.

To define $p(\{f_i\}|\boldsymbol{z}_{W,3D})$, we follow the approach developed by *Chen et al.* [2006]. Here $\{f_i\}$ is an indicator field such that the facies at each element f_i has a Bernoulli distribution given by:

$$p(f_i=1|\boldsymbol{z}_{W,3D},\{f_{i,k\neq i}\})=\text{Bernoulli}(p_i^*), \tag{4}$$

where p_i^* can be determined by simple indicator kriging:

$$p_i^*=\mu+\sum_{k\neq i}c_k(f_k-\mu), \tag{5}$$

where μ is the overall mean. Note that p_i is truncated within [0, 1]. The kriging coefficients c_k's are a function of the correlation length and sill, derived from the exponential variogram model, and the distance between Pixel *k* and Pixel *i*. In this study, we assume that they are fixed and determined by the variogram analysis.

We use MCMC methods to sample from the joint posterior distribution $p(\{f_i\}|\,\boldsymbol{r},\boldsymbol{\phi},\boldsymbol{z}_{W,3D})$, which is the marginal distribution of $p(\{f_i\},\boldsymbol{\alpha}|\,\boldsymbol{r},\boldsymbol{\phi},\boldsymbol{z}_{W,3D})$. The MCMC sampling requires formulation of the probability distribution of each parameter conditioned on the other parameters and all data sets. We sample the indicator at each pixel f_i.

$$p(f_i|\boldsymbol{r},\boldsymbol{\phi},\boldsymbol{z}_{W,3D},\{f_{k,k\neq i}\},\boldsymbol{\alpha})\propto p(r_i,\phi_i|f_i,\boldsymbol{\alpha})p(f_i|\boldsymbol{z}_{W,3D},\{f_{k,k\neq i}\}). \tag{6}$$

With a mathematical manipulation similar to that used in *Chen et al.* [2006], we can arrive at an analytical form of the distribution. The indicator f_i follows a Bernoulli distribution with the probability:

$$p(f_i=1|r_i,\phi_i,\{f_{k,k\neq i}\},\boldsymbol{\alpha},\boldsymbol{z}_{W,3D})=\frac{p_1p_i^*}{p_1p_i^*+p_0(1-p_i^*)}. \tag{7}$$

where $p_0=p(r_i,\phi_i|f_i=0,\Phi_0)$ and $p_1=p(r_i,\phi_i|f_i=1,\Phi_1)$, both of which are defined in equation (2) and represent likelihood information from the IP data.

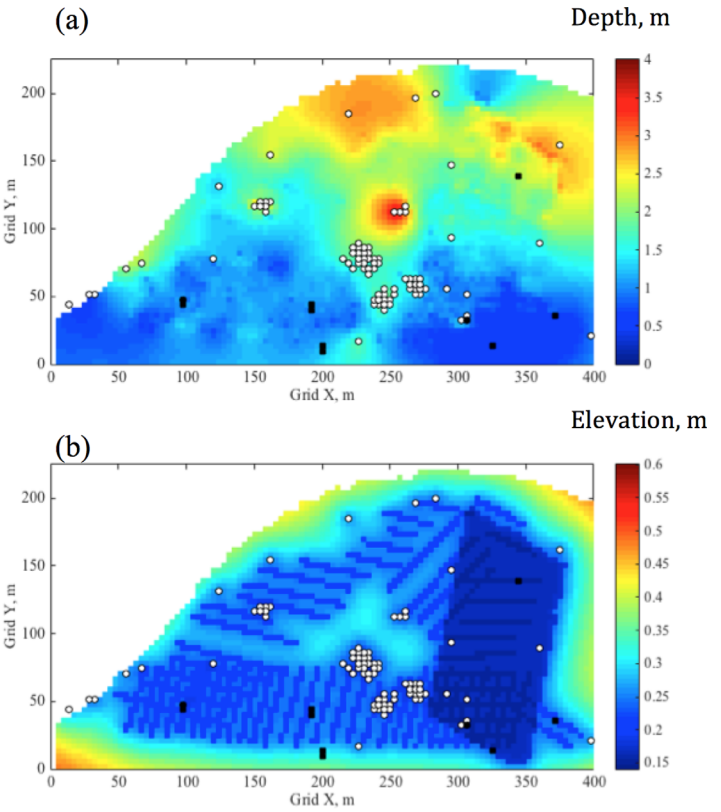

Figure 7. Fill-Rifle Interface estimation results: (a) the mean estimate of the depth in meters and (b) the variance in squared meters. The white circles are the well locations used for the estimation, and the black circles are the well locations used for validation.

To sample the covariance matrices in $\boldsymbol{\alpha}$ (Φ_0 and Φ_1), we follow a similar approach to the univariate case developed by *Chen et al.* [2006]. While *Chen et al.* [2006] used the inverse gamma distribution as a conjugate prior, we use the Wishart distribution, which is multidimensional generalization of the inverse gamma distribution [*Murphy*, 2007]. We assume that the prior distribution for each of the covariance matrices (Φ_0 and Φ_1) is an inverse Wishart distribution with the degree of freedom m_0 and m_1, and the inverse-scale matrices Ψ_0 and Ψ_1, respectively. We determined these parameters from the colocated data sets shown in Figure 4b [*Chen et al.*, 2006]. Since the inverse Wishart distribution is a conjugate prior for the covariance of a multivariate normal distribution, the posterior of Φ_0 and Φ_1 are defined by the inverse Wishart distribution (*IW*):

$$p(\Phi_l|\bullet) \sim IW\left(m_l+n_l, X^T X\right), \tag{8}$$

where $X = \{\boldsymbol{r} - \mathrm{E}[\boldsymbol{r}], \boldsymbol{\phi} - \mathrm{E}[\boldsymbol{\phi}]\}$ ($\mathrm{E}[\cdot]$ is the mean), n_l is the number of IP data locations where $f_i = l$ ($l = 0$ or 1). In the MCMC sequence, we sample each pixel of $\{f_i\}$ and $\boldsymbol{\alpha}$ sequentially. Since their conditional distributions are

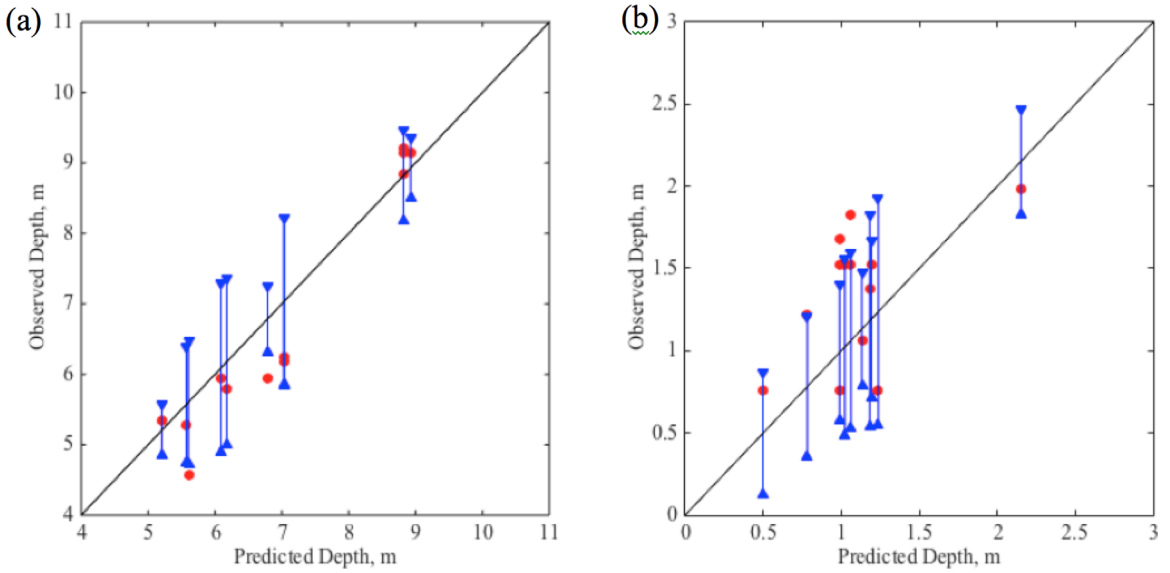

Figure 8. Estimated mean and confidence interval compared with the interpretations from the well data not used in the estimation; (a) the Rifle-Wasatch interface depth and (b) Rifle-Fill interface depth. The red dots represent the interfaces at wells, the blue lines are the confidence intervals based on the standard deviation (STD) multiplied by two, and the black lines are the one-to-one line.

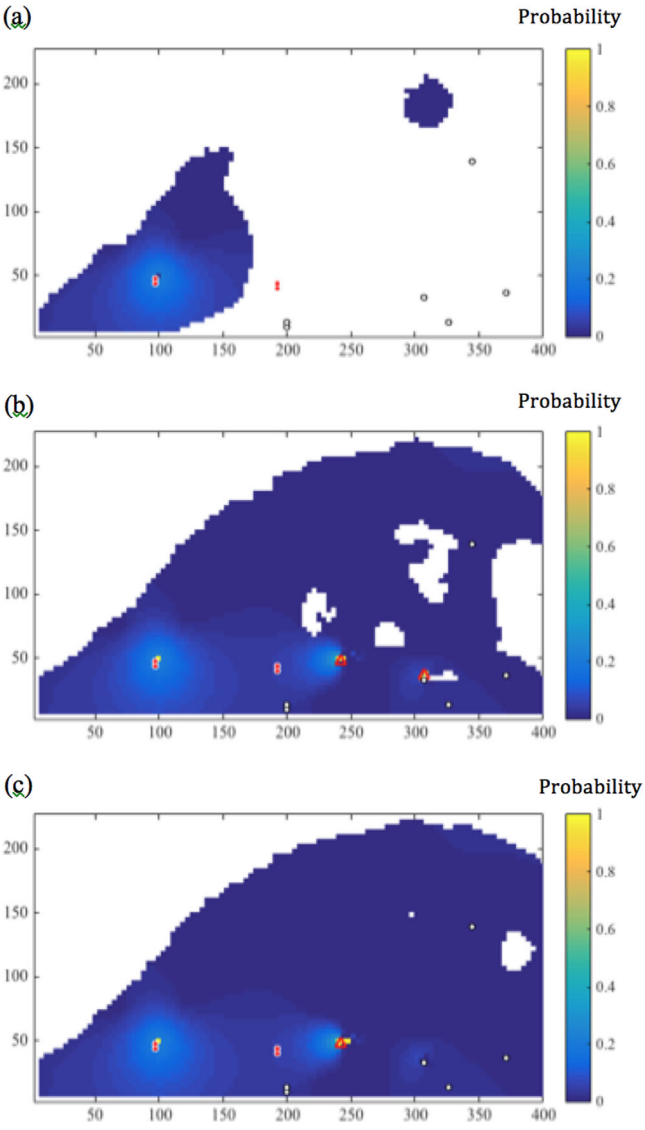

Figure 9. Probability field of NRZs based on well data only; 2-D horizontal slices at elevations (a) 1611.6 m, (b) 1613.2 m, and (c) 1613.8 m. The red filled circles are the wells that were confirmed to have NRZs, and the white circles are the wells that were confirmed not to have NRZs. These are validation wells, not included in the estimation. The red triangles were the NRZ sample locations in *Campbell et al.* [2012] and *Qafoku et al.* [2014]. The white region is either outside of the domain or outside of the Rifle Formation.

known analytical distributions, we use Gibbs sampling, which is quite efficient compared to the other MCMC sampling methods.

5. Estimation Results and Discussions

5.1. Interface Estimation

We estimated the interfaces at each grid in the domain as needed for input into a biogeochemical model over the floodplain. The grid size is 3.8 m by 3.8 m, and the domain size is 400 m by 229 m. For the Rifle-Wasatch interface, there is a previously estimated interface elevation available, which is based on well data, outcrop, and geological observations. We estimated the difference from these previous estimates, by honoring the outcrop and geological observations, as well as wellbore and geophysical data. For the estimation, we only computed the mean and variance fields on the interfaces, rather than random fields, since most reactive transport models require fixed interfaces. However, it is possible to sample the random fields of the interfaces for stochastic simulations to include the uncertainty in interface estimates.

Figure 6 shows the Rifle-Wasatch interface elevation, including the previously estimated elevation (Figure 6a), mean estimation of the elevation (Figure 6b), and the mean estimation of depths and variance (Figure 6c). Compared to the previous estimation (Figure 6a), the new estimation (Figure 6b) captures more detailed heterogeneity around the ERT locations, even between wells. In addition, ERT identified the connectivity (or channel) between the depressions in the Rifle-Wasatch interface along the northern part of this floodplain ($x = 250$–350 m and $y = 150$–200 m). We interpret this channel to represent a former paleochannel of the Colorado River and a potential local control on groundwater flow direction in this area. The Wasatch Formation depth (Figure 6c) is highly variable (4–10 m) over the floodplain. The variance in Figure 6d represents the uncertainty associated with this mean estimate. This variance is smaller around the wells and ERT locations, since the estimate is better constrained by the data sets in their vicinity.

Figure 7 shows the mean estimate and variance of the Rifle-fill interface depth. In Figure 7a, we find that the fill layer is thicker in the northern portion of the floodplain, where soil contamination extended over a greater vertical profile. The southern portion near the river has a thinner layer reflecting the minimal need for excavation and removal of surficial soils in this area. In Figure 7b, the estimation variance is smaller near the ERT and IP data locations, meaning that there is lower uncertainty in the estimate for this region. Owing to its lower permeability, the fill layer is known to control infiltration into groundwater as well as evapotranspiration near the

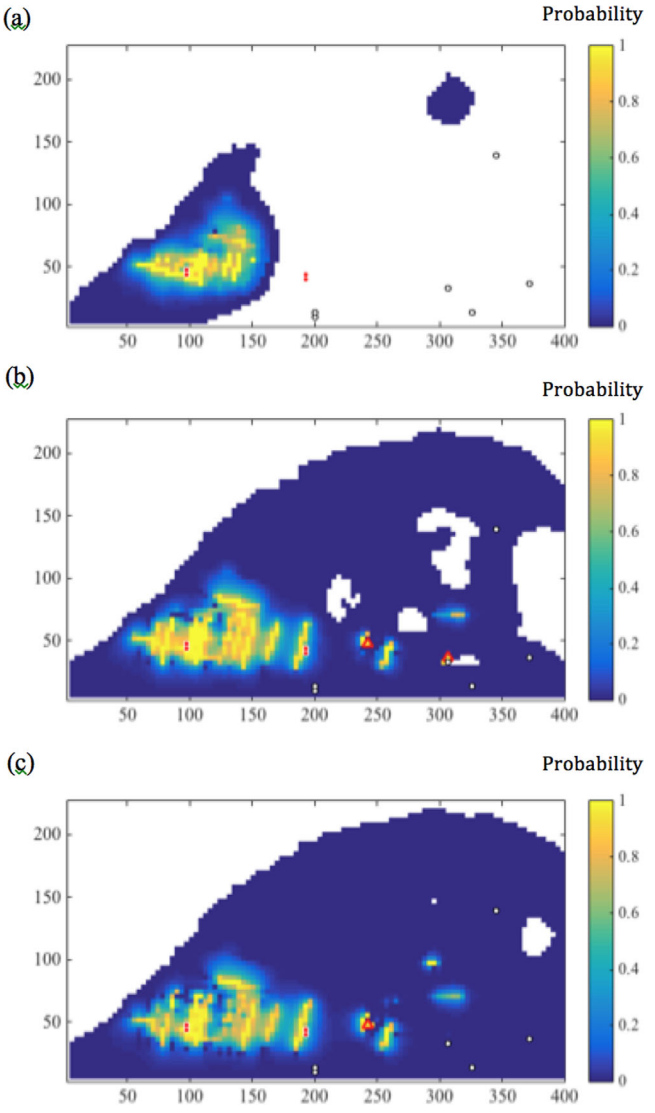

Figure 10. Posterior probability field of NRZs based on wells and TDIP data; 2-D horizontal slices at elevations (a) 1611.6 m, (b) 1613.2 m, and (c) 1613.8 m. The red filled circles are the wells that were confirmed to have NRZs (based on well-bore lithology), and the white circles are the wells that were confirmed not to have NRZs. These are validation wells, not included in the estimation. The red triangles were the NRZ sample locations in *Campbell et al*. [2012] and *Qafoku et al*. [2014]. The white region is either outside of the domain or outside of the Rifle Formation.

surface. Since there is no record of the fill-layer thickness postreclamation, this newly derived, site-wide thickness estimate will be important for hydrobiogeochemical modeling at the site.

To validate the estimation results, Figure 8 shows a comparison of the estimated interface mean value and confidence interval, with the colocated (well-determined) interfaces not used in the estimation procedure. Among the 187 wells, 16 new wells (installed in 2014) were selected as validation wells (not used for estimation). We did not use this subset of wells for our estimation in order to simulate the situation that researchers would encounter when they plan well locations based on geophysical images and estimation results. The Wasatch depths (Figure 8a) are closely estimated at most of the locations (i.e., the confidence intervals capture the true depths), although the confidence intervals are larger for the wells that are away from the existing wells or ERT locations. Figure 8b shows that the true fill depth at the validation points is close to the mean estimates and mostly within the confidence intervals. Confidence intervals are wider for the validation wells far away from the conditioning wells or geophysical data. The comparison of the two figures suggests that the resistivity method is useful—indeed necessary—to estimate the spatially heterogeneous interfaces successfully.

5.2. NRZ Estimation Results

The presence or absence of NRZs was estimated within a 3-D hydrobiogeochemical modeling domain being developed in parallel to this study. Only the cells within the Rifle Formation were considered, based on the interfaces estimated in Figures 6 and 7. Geostatistical parameters (i.e., mean, variance, and correlation length) were determined based on the lithological logs. We used the MCMC approach to generate 20,000 samples of the NRZ indicator field, the convergence of which was confirmed by the Geweke's convergence diagnostic [*Geweke*, 1992]. Wells installed prior to 2013 were used as conditioning data in the estimation, with 16 new wells installed in 2014 used as validation data to evaluate the performance of the estimation.

We compared two cases in the results: (1) well data only (Figure 9) and (2) well and TDIP data (Figure 10). In Figure 9, we see that the well-only case does not capture any of the major NRZs due to the lack of data. Capturing the full NRZ extent would require installation of innumerable wells at a cost that is prohibitive or logistically impossible. In Figure 10, including TDIP data allows us to capture the extent of NRZs, particularly in the western portion of the floodplain near the river ($x = 50$–200 m and $y = 30$–100 m). The additional high-probability regions appeared in Figure 10 (compared to Figure 9) is attributed to the TDIP data set. The results indicate that

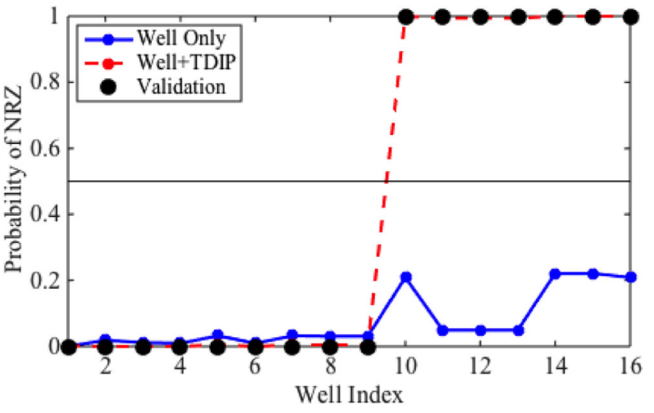

Figure 11. Probability of finding NRZs at each validation well. The lines are the probability computed based on well data only (blue) and bivariate data (phase shift and resistivity; red). The black dots represent the observations not used in the estimation; the value is 1 if the well is located within a NRZ, and 0 otherwise.

NRZs are generally located in proximity to the active river margin and in portions of the aquifer where the depth to the Wasatch Formation is deeper (Figure 6).

To evaluate the performance of our estimation, we compared the predicted NRZ probabilities and observed NRZ indicators at the validation well locations. In Figure 11, the probability of finding an NRZ at each well is shown and compared with the indicator representing whether an NRZ was found at the well. The figure shows that when we used both wellbore and TDIP data, the probability is one or close to one at all the observed NRZ locations and zero or close to zero at the observed non-NRZ locations. The well-only case does not capture any of the NRZ locations, since the probability is zero at those locations. These findings support the claim that it is impossible to characterize the full spatial extent of NRZs with well data only and that IP measurements greatly improve the mapping of NRZs.

Figure 12 shows the 3-D distribution of the high-probability region of NRZs (with threshold of 0.5) along with the two estimated interfaces. Both the interfaces and NRZ locations can be directly implemented in hydrobiogeochemical simulations serving to parameterize the modeling domain with regions inferred to have an outsized influence on reactions of interest (e.g., hot spot locations). In Figures 10 and 12, we find that the NRZs are generally parallel to and located 20–50 m from the active margin of the Colorado River (N.B. Closer access to the active river margin itself is impeded due to the presence of a railway corridor). Previous studies [*Campbell et al.*, 2012; *Qafoku et al.*, 2014; *Janot et al.*, 2015] found close association between NRZs and fine and/or organic-rich sediments. In fact, fine-grained and organic-rich sediments are often found near the river, based on the lithological descriptions. Based on this study, we may assume that those identified NRZ locations are the regions where fine-grained sediments were deposited.

6. Conclusion

In this study, we developed a methodology to integrate geophysical and wellbore data for mapping naturally reduced zones (NRZs) in a minimally invasive manner and to help biogeochemical model parameterization in a three-dimensional domain over a floodplain. Our study builds upon previous studies at the site that identified NRZs using detailed geochemical and microbial characterization [*Campbell et al.*, 2012; *Qafoku et al.*, 2014], as well as studies that used IP techniques to detect changes in subsurface redox conditions [*Williams et al.*, 2009; *Flores Orozco et al.*, 2011, 2013; *Chen et al.*, 2013]. Our approach took advantage of the data-defined correlations among colocated geochemical samples, lithological log data, and geophysical data. A Bayesian hierarchical method enabled us to integrate these data for

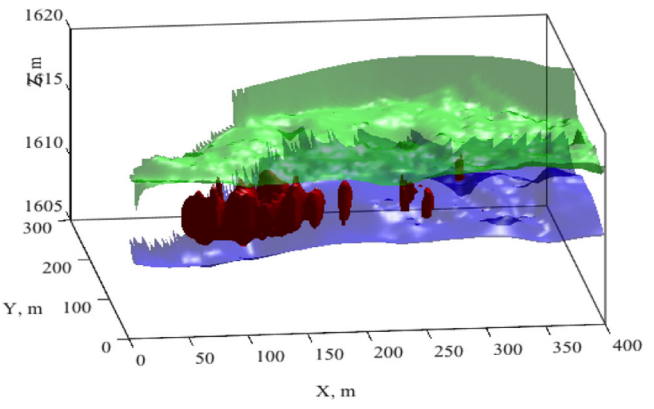

Figure 12. A three-dimensional modeling domain with the Rifle-Fill interface (green), Wasatch-Rifle interface (blue), and the high-probability region of naturally reduced zones (NRZs; red). To create the volume of the high-probability region, we used the threshold probability of 0.5.

estimating the hydrostratigraphic interfaces, as well as the probability of NRZ presence or absence over the dimensions of the floodplain. This is the first study to demonstrate the ability of TDIP imaging surveys for characterizing hot spots that have unique distributions of subsurface lithological and biogeochemical properties.

Many recent studies use Bayesian or stochastic joint inversion approaches to estimate hydrological parameters or geological units directly from geophysical data sets by including geophysical forward models in the estimation framework [e.g., *Chen et al*., 2004; *Chen and Hoversten*, 2012; *Dafflon and Barrash*, 2012; *Wainwright et al*., 2014; *Hermans et al*., 2015]. Such approaches, however, are computationally intensive and difficult to deploy in a 3-D setting over a large spatial domain. The two-step approach presented here—geophysical inversion first and then estimation along with other data sets—is flexible and computationally frugal enough to integrate multiple types of data sets together in a 3-D domain over a floodplain. Statistical analyses at colocated wells enabled us to identify correlations between inverted data and borehole data. This study also showed that it is important to evaluate various polarization-generating mechanisms for an improved interpretation of IP images particularly where the unambiguous delineation of NRZs is concerned.

As with the previous studies [*Sassen et al*., 2012; *Wainwright et al*., 2014], this study showed that the zonation approach is very powerful in transferring the information and parameters from grain-scale laboratory measurements to the field scale. Detailed biogeochemical characterization is often prohibitively expensive and time consuming, such that it is generally impossible to obtain sufficient data to fully constrain many natural environments owing to their large size and inherent heterogeneity. By exploiting spatially extensive geophysical data sets and correlations among various data sets, we can capture the subsurface heterogeneity required for parameterizing hydrobiogeochemical models.

The approach developed in this study can be transferable to other floodplains or other near-surface terrestrial environments, advancing the characterization of biogeochemical hot spots in a minimally invasive manner and distributing critical biogeochemical properties across scales. Future development should include the use of geophysical monitoring to use a temporal signature for estimating dynamic properties associated with NRZs and non-NRZs (such as changes in pore water chemistry) and also for further refining the estimation of hydraulic and geochemical properties (e.g., permeability, porosity, and texture). Another important refinement will be to couple geophysical methods and remote sensing techniques. While the denitrification hot spots by *Duncan et al*. [2013] have been mapped in 2-D as an "area" over the catchment, geophysical methods could provide more refined estimates of their depth distribution, and hence could provide the 3-D volume of biogeochemical hot spots. Although the IP measurements presented here are labor intensive and are unlikely to be taken to the catchment scale, correlating the subsurface signatures (from geophysical data) and surface structures (from remote sensing data) could help upscaling the subsurface properties to a much larger scale [e.g., *Wainwright et al*., 2015]. Probabilistic mapping—such as the one presented here—will be essential for such a large-scale characterization due to increased uncertainty and disparity of scales among data sets.

Appendix A: Analytical Form of $p(\{d_i\}|\boldsymbol{z}_{ERT}, \boldsymbol{z}_{IP}, \boldsymbol{z}_L)$

To estimate the posterior distribution of the interface $\{d_i\}$, we derive the analytical form of $p(\{d_i\}|\boldsymbol{z}_{ERT}, \boldsymbol{z}_{IP}, \boldsymbol{z}_L)$ defined in section 2.1. Following the data model definition, we write the ERT and IP data vector by

$$\begin{aligned} \boldsymbol{z}_{ERT} &\sim \mathrm{MVN}(\mathrm{A}_{ERT}\{d_i\}, \mathrm{D}_{ERT}), \\ \boldsymbol{z}_{IP} &\sim \mathrm{MVN}(\mathrm{A}_{IP}\{d_i\}, \mathrm{D}_{IP}), \end{aligned} \tag{A1}$$

where MVN represents the multivariate normal distribution, and D_{ERT} and D_{IP} are the data error matrices, only having the diagonal components of σ_{ERT} and σ_{IP}, respectively. A_{ERT} and A_{IP} are sparse matrices to connect the interface depth value at each pixel and the data point such that

$$\mathrm{A}_{ERT,ji} = \begin{cases} 1 & \text{if } i\text{th pixel is } j\text{th ERT data point} \\ 0 & \text{otherwise.} \end{cases}$$

and

$$A_{IP\,ji} = \begin{cases} 1 & \text{if } i\text{th pixel is } j\text{th IP data point} \\ 0 & \text{otherwise} \end{cases}. \tag{A2}$$

We can write the posterior distribution of the interface as:

$$\begin{aligned} p(\{d_i\}|\boldsymbol{z}_{ERT}, \boldsymbol{z}_{IP}, \boldsymbol{z}_L) &\propto p(\boldsymbol{z}_{ERT}|\{d_i\})p(\boldsymbol{z}_{IP}|\{d_i\})p(\{d_i\}|\boldsymbol{z}_L), \\ &\propto \exp\left[-\frac{1}{2}\left(\boldsymbol{z}_{ERT} - A_{ERT}\{d_i\}\right)^T D_{ERT}^{-1}\left(\boldsymbol{z}_{ERT} - A_{ERT}\{d_i\}\right)\right] \\ &\exp\left[-\frac{1}{2}\left(\boldsymbol{z}_{IP} - A_{IP}\{d_i\}\right)^T D_{IP}^{-1}\left(\boldsymbol{z}_{IP} - A_{IP}\{d_i\}\right)\right]\exp\left[-\frac{1}{2}(\{d_i\} - \boldsymbol{\mu}_c)^T \Sigma_c^{-1}(\{d_i\} - \boldsymbol{\mu}_c)\right]. \end{aligned} \tag{A3}$$

Since both ERT and IP data are linear functions of interface depths according to equations (A1) and (A2), the resultant posterior distribution has a multivariate Gaussian distribution, which is given below:

$$p(\{d_i\}|\boldsymbol{z}_{ERT}, \boldsymbol{z}_{IP}, \boldsymbol{z}_L) \propto \exp\left[-\frac{1}{2}\left(\{d_i\} - Q^{-1}\boldsymbol{g}\right)^T Q\left(\{d_i\} - Q^{-1}\boldsymbol{g}\right)\right]. \tag{A4}$$

where

$$\begin{aligned} Q &= \Sigma_c^{-1} + A_{ERT}^T D_{ERT}^{-1} A_{ERT} + A_{IP}^T D_{IP}^{-1} A_{IP}, \\ g &= \Sigma_c^{-1}\boldsymbol{\mu}_c + A_{ERT} D_{ERT}^{-1}\boldsymbol{z}_{ERT} + A_{IP} D_{IP}^{-1}\boldsymbol{z}_{IP}, \end{aligned} \tag{A5}$$

$\{d_i\}$ is the multivariate normal distribution with the mean $Q^{-1}g$ and covariance Q^{-1}.

Acknowledgment
This material is partially based upon work supported through the Lawrence Berkeley National Laboratory's Sustainable Systems Scientific Focus Area (SFA). The U.S. Department of Energy (DOE), Office of Science, and Office of Biological and Environmental Research funded the work under contract DE-AC02-05CH11231 (Lawrence Berkeley National Laboratory; operated by the University of California). We would like to thank Joel Rowland at Los Alamos National Laboratory for providing advice that helped to strengthen the conceptual model of floodplain-related hot spots. Data sets are available upon request by contacting the corresponding author (Haruko M. Wainwright, hmwainwright@lbl.gov).

References

Abdel Aal, G. Z., E. A. Atekwana, and A. Revil (2014), Geophysical signatures of disseminated iron minerals: A proxy for understanding subsurface biophysicochemical processes, *J. Geophys. Res. Biogeosci.*, *119*, 1831–1849, doi:10.1002/2014JG002659.

Anderson, T., P. Groffman, and M. Walter (2015), Using a soil topographic index to distribute denitrification fluxes across a northeastern headwater catchment, *J. Hydrol.*, *522*, 123–134, doi:10.1016/j.jhydrol.2014.12.043.

Archie, G. (1942), The electrical resistivity log as an aid in determining some reservoir characteristics, *Trans. AIME*, *146*, 54–62.

Arora, B., et al. (2015a), Influence of hydrological, biogeochemical and temperature transients on subsurface carbon fluxes in a flood plain Environment, *Biogeochemistry*, doi:10.1007/s10533-016-0186-8, in press.

Arora, B., D. Dwivedi, N. F. Spycher, and C. I. Steefel (2015b), Modeling processes affecting carbon dynamics at a biogeochemical hotspot in a floodplain aquifer, in *Proceedings of the TOUGH Symposium 2015*, pp. 456–463, Lawrence Berkeley National Laboratory, Berkeley, Calif.

Aufdenkampe, A. K., E. Mayorga, P. A. Raymond, J. M. Melack, S. C. Doney, S. R. Alin, and K. Yoo (2011), Riverine coupling of biogeochemical cycles between land, oceans, and atmosphere, *Frontiers Ecol. Environ.*, *9*(1), 53–60.

Battin, T. J., L. A. Kaplan, S. Findlay, C. S. Hopkinson, E. Marti, A. I. Packman, J. D. Newbold, and F. Sabate (2008), Biophysical controls on organic carbon fluxes in fluvial networks, *Nat. Geosci.*, *1*(2), 95–100, doi:10.1038/ngeo101.

Battin, T. J., S. Luyssaert, L. A. Kaplan, A. K. Aufdenkampe, A. Richter, and L. J. Tranvik (2009), The boundless carbon cycle, *Nat. Geosci.*, *2*(9), 598–600, doi:10.1038/ngeo618.

Binley, A., and A. Kemna (2005), DC resistivity and induced polarization methods, in *Hydrogeophysics*, edited by Y. Rubin and S. Hubbard, pp. 129–156, Springer, Dordrecht, Netherlands, doi:10.1007/1-4020-3102-5_5.

Binley, A., L. D. Slater, M. Fukes, and G. Cassiani (2005), Relationship between spectral induced polarization and hydraulic properties of saturated and unsaturated sandstone, *Water Resour. Res.*, *41*, W12417, doi:10.1029/2005WR004202.

Binley, A., S. S. Hubbard, J. A. Huisman, A. Revil, D. A. Robinson, K. Singha, and L. D. Slater (2015), The emergence of hydrogeophysics for improved understanding of subsurface processes over multiple scales, *Water Resour. Res.*, *51*, 3837–3866, doi:10.1002/2015WR017016.

Blaschek, R., A. Hördt, and A. Kemna (2008), A new sensitivity-controlled focusing regularization scheme for the inversion of induced polarization data based on the minimum gradient support, *Geophysics*, *73*, F45−F54.

Börner, F. D., J. R. Schopper, and A. Weller (1996), Evaluation of transport and storage properties in the soil and groundwater zone from induced polarization measurements, *Geophys. Prospect.*, *44*, 583–601, doi:10.1111/j.1365-2478.1996.tb00167.x.

Bowling, J. C., A. B. Rodriguez, D. L. Harry, and C. Zheng (2005), Delineating alluvial aquifer heterogeneity using resistivity and GPR data, *Ground Water*, *43*(6), 890–903.

Bücker, M., and A. Hördt (2013), Analytical modelling of membrane polarization with explicit parametrization of pore radii and the electrical double layer, *Geophys. J. Int.*, *194*(2), 804–813.

Campbell, K. M., et al. (2012), Characterizing the extent and role of natural subsurface bioreduction in a uranium-contaminated aquifer, *Appl. Geochem.*, *27*, 1499–1511.

Capps, K., R. Rancatti, N. Tomczyk, T. Parr, A. Calhoun, and M. Hunter (2014), Biogeochemical hotspots in forested landscapes: The role of vernal pools in denitrification and organic matter processing, *Ecosystems*, *17*(8), 1455–1468, doi:10.1007/s10021-014-9807-z.

Castelle, C. J., L. A. Hug, K. C. Wrighton, B. C. Thomas, K. H. Williams, D. Wu, S. G. Tringe, S. W. Singer, J. A. Eisen, and J. F. Banfield (2013), Extraordinary phylogenetic diversity and metabolic versatility in aquifer sediment, *Nat. Commun.*, *4*, 2120.

Caterina, D., T. Hermans, and F. Nguyen (2014), Case studies of incorporation of prior information in electrical resistivity tomography: Comparison of different approaches, *Near Surf. Geophys.*, *12*(4), 451–465.

Chen, J., and M. Hoversten (2012), Joint inversion of marine seismic AVA and CSEM data using statistical rock-physics models and Markov random fields, *Geophysics*, *77*, R65–R80, doi:10.1190/GEO2011-0219.1.

Chen, J., S. Hubbard, Y. Rubin, C. Murray, E. Roden and E. Majer (2004), Geochemical characterization using geophysical data and Markov chain Monte Carlo methods: A case study at the South Oyster Bacterial Transport Site in Virginia, *Water Resour. Res.*, *40*, W12412, doi: 10.1029/2003WR002883.

Chen, J., S. S. Hubbard, J. E. Peterson, K. Williams, M. Fienen, P. Jardine, and D. Watson (2006), Development of a joint hydrogeophysical inversion approach and application to a contaminated fractured aquifer, *Water Resour. Res.*, *42*, W06425, doi:10.1029/2005WR004694.

Chen, J., S. S. Hubbard, and K. H. Williams (2013), Data-driven approach to identify field-scale biogeochemical transitions using geochemical and geophysical data and hidden Markov models: Development and application at a uranium-contaminated aquifer, *Water Resour. Res.*, *49*, 6412–6424, doi:10.1002/wrcr.20524.

Cole, J., et al. (2007), Plumbing the global carbon cycle: Integrating inland waters into the terrestrial carbon budget, *Ecosystems*, *10*, 172–185.

Dafflon, B., and W. Barrash (2012), Three-dimensional stochastic estimation of porosity distribution: Benefits of using ground-penetrating radar velocity tomograms in simulated-annealing-based or Bayesian sequential simulation approaches, *Water Resour. Res.*, *48*, W05553, doi:10.1029/2011WR010916.

Doetsch, J., N. Linde, M. Pessognelli, A. G. Green, and T. Günther (2012), Constraining 3-D electrical resistance tomography with GPR reflection data for improved aquifer characterization, *J. Appl. Geophys.*, *78*, 68–76.

Duncan, J., P. Groffman, and L. Band (2013), Towards closing the watershed nitrogen budget: Spatial and temporal scaling of denitrification, *J. Geophys. Res. Biogeosci.*, *118*, 1105–1119, doi:10.1002/jgrg.20090.

Flores Orozco, A., K. H. Williams, P. E. Long, S. S. Hubbard and A. Kemna (2011), Using complex resistivity imaging to infer biogeochemical processes associated with bioremediation of a uranium-contaminated aquifer, *J. Geophys. Res.*, *116*, G03001, doi:10.1029/2010JG001591.

Flores Orozco A., A. Kemna, C. Oberdörster, L. Zschornack, C. Leven, P. Dietrich, and H. Weiss (2012a), Delineation of subsurface hydrocarbon contamination at a former hydrogenation plant using spectral induced polarization imaging, *J. Contam. Hydrol.*, *136–137*, 131–144.

Flores Orozco, A., A. Kemna, and E. Zimmermann (2012b), Data error quantification in spectral induced polarization imaging, *Geophysics*, *77*(3), E227–E237.

Flores Orozco, A., K. H. Williams, and A. Kemna (2013), Time-lapse spectral induced polarization imaging of stimulated uranium bioremediation, *Near Surf. Geophys.*, *11*(1988), 531–544, doi:10.3997/1873-0604.2013020.

Geweke, J. (1992), Evaluating the accuracy of sampling-based approaches to calculating posterior moments, in *Bayesian Statistics*, vol.4, edited by J. M. Bernado et al., pp. 169–193, Clarendon, Oxford, N. Y.

Grimm, N. B., et al. (2003), Merging aquatic and terrestrial perspectives of nutrient biogeochemistry, *Oecologia*, *137*, 485–501.

Gomez, J. D., J. L. Wilson, and M. B. Cardenas (2012), Residence time distributions in sinuosity-driven hyporheic zones and their biogeochemical effects, *Water Resour. Res.*, *48*, W09533, doi:10.1029/2012WR012180.

Hedin, L. O., J. C. Fischer, N. E. Ostrom, B. P. Kennedy, M. G. Brown, and P. G. Robertson (1998), Thermodynamic constraints on nitrogen transformations and other biogeochemical processes at soil-stream interfaces, *Ecology*, *79*(2), 684–703, doi:10.1890/0012-9658(1998)079.

Heimann, M., and M. Reichstein (2009), Terrestrial ecosystem carbon dynamics and climate feedbacks, *Nature*, *451*, 289–292.

Hermans, T., F. Nguyen, and J. Caers (2015), Uncertainty in training image-based inversion of hydraulic head data constrained to ERT data: Workflow and case study, *Water Resour. Res.*, *51*, 5332–5352, doi:10.1002/2014WR016460.

Hill, A. R., K. J. Devito, S. Campagnolo, and K. Sanmugadas (2000), Subsurface denitrification in a forest riparian zone: Interactions between hydrology and supplies of nitrate and organic carbon, *Biogeochemistry*, *51*(2), 193–223.

Holmes, R. M., J. B. Jones Jr., S. G. Fisher, and N. B. Grimm (1996), Denitrification in a nitrogen-limited stream ecosystem, *Biogeochemistry*, *33*(2), 125–146.

Hubbard, S. S., and N. Linde (2011), Hydrogeophysics, in *Treatise on Water Science*, vol. 2, edited by P. Wilderer, Academic, Oxford, U. K.

Hubbard, S. S., J. Chen, J. E. Peterson, E. Majer, K. W. Williams, D. Swift, B. Mailliox, and Y. Rubin (2001), Hydrogeological characterization of the D.O.E. bacterial transport site in Oyster Virginia using geophysical data, *Water Resour. Res.*, *37*(10), 2431–2456.

Janot, N., et al. (2015), Physico-chemical heterogeneity of organic-rich sediments in the Rifle aquifer, CO: Impact on uranium biogeochemistry, *Environ. Sci. Technol.*, *50*(1), 46–53, doi:10.1021/acs.est.5b03208.

Johnston, C. A., S. D. Bridgham, and J. P. Schubauer-Berigan (2001), Nutrient dynamics in relation to geomorphology of riverine wetlands, *Soil Sci. Soc. Am. J.*, *65*(2), 557–577.

Kemna, A. (2000), Tomographic inversion of complex resistivity: Theory and application, PhD thesis, Ruhr Univ., Bochum, Germany.

Kemna, A., E. Räkers, and A. Binley (1997), Application of complex resistivity tomography to field data from a Kerosene-contaminated site, in *Proceedings of 3rd Meeting of Environmental and Engineering Geophysics Society, Environ. Eng. Geophys. Soc.*, pp. 151–154, Denver, Colo.

Kennedy, D. O., C. Leven, and O. A. Cirpka (2013), Delineating subsurface heterogeneity at a loop of River Steinlach using geophysical and hydrogeological methods, *Environ. Earth Sci.*, *69*(2), 335–348.

Kowalsky, M. B., E. Gasperikova, S. Finsterle, D. Watson, G. Baker, and S. S. Hubbard (2011), Coupled modeling of hydrogeochemical and electrical resistivity data for exploring the impact of recharge on subsurface contamination, *Water Resour. Res.*, *47*, W02509, doi: 10.1029/2009WR008947.

LaBrecque, D., and W. Daily (2008), Assessment of measurement errors for galvanic-resistivity electrodes of different composition, *Geophysics*, *73*(2), F55–F64.

Marshall, D. J., and T. R. Madden (1959), Induced polarization, a study of its causes, *Geophysics*, *24*(4), 790–816.

McClain, M., et al. (2002), Biogeochemical hot spots and hot moments at the interface of terrestrial and aquatic ecosystems, *Ecosystems*, *6*, 301–312, doi:10.1007/s10021-003-0161-9.

Melack, J. (2011), Biogeochemistry: Riverine carbon dioxide release, *Nat. Geosci.*, *4*, 821–822.

Mouser, P. J., et al. (2014), Influence of carbon and microbial community priming on the attenuation of uranium in a contaminated floodplain aquifer, *Ground Water*, *53*, 600–613, doi:10.1111/gwat.12238.

Murphy, K. P. (2007), Conjugate Bayesian analysis of the Gaussian distribution, technical report. [Available at http://wwwdevel.cs.ubc.camurphyk/Papers/bayesGauss.pdf.]

Mwakanyamale, K., L. Slater, A. Binley, and D. Ntarlagiannis (2012), Lithologic imaging using induced polarization: Lessons learned from the Hanford 300 area, *Geophysics*, *77*, 397–409.

Neff, J. C., and G. P. Asner (2001), Dissolved organic carbon in terrestrial ecosystems: Synthesis and a model, *Ecosystems*, *4*, 29–48.

Nguyen, F., et al. (2009), Characterization of seawater intrusion using 2D electrical imaging, *Near Surface Geophysics*, *7*, 377–390.

Ntarlagiannis, D., K. H. Williams, L. D. Slater, and S. S. Hubbard (2005), Low frequency electrical response to microbial induced sulfide precipitation, *J. Geophys. Res.*, *110*, G02009, doi:10.1029/2005JG000024.

Pelton, W. H., S. H. Ward, P. G. Hallof, W. R. Sill, and P. H. Nelson (1978), Mineral discrimination and removal of inductive coupling with multifrequency IP, *Geophysics*, *43*(3), 588–609.
Qafoku, N. P., et al. (2014), Geochemical and mineralogical investigation of uranium in multi-element contaminated, organic-rich subsurface sediment, *Appl. Geochem.*, *42*, 77–85, doi:10.1016/j.apgeochem.2013.12.001.
Revil, A., and N. Florsch (2010), Determination of permeability from spectral induced polarization in granular media, *Geophys. J. Int.*, *181*, 1480–1498.
Rubin, Y., and S. S. Hubbard (Eds.) (2005), *Hydrogeophysics*, vol. 50, Springer, Berlin.
Sassen, D. S., S. S. Hubbard, S. A. Bea, J. Chen, N. Spycher, and M. E. Denham (2012), Reactive facies: An approach for parameterizing field-scale reactive transport models using geophysical methods, *Water Resour. Res.*, *48*, W10526, doi:10.1029/2011WR011047.
Scheibe, T. D., and D. L. Freyberg (1995), Use of sedimentological information for geometric simulation of natural porous media structure, *Water Resour. Res.*, *31*(12), 3259–3270, doi:10.1029/95WR02570.
Schindler, J. E., and D. P. Krabbenhoft (1998), The hyporheic zone as a source of dissolved organic carbon and carbon gases to a temperate forested stream, *Biogeochemistry*, *43*(2), 157–174.
Scott, J. B. T., and R. D. Barker (2003), Determining pore-throat size in Permio-Triassic sandstones from low-frequency electrical spectroscopy, *Geophys. Res. Lett.*, *30*(9), 1450, doi:10.1029/2003GL016951.
Slater, D. L., D. Choi, and Y. Wu (2005), Electrical properties of iron-sand columns: Implications for induced polarization investigation and performance monitoring of iron wall barriers, *Geophysics*, *70*(4), G87–G94.
Slater, L., and A. Binley, 2006, Synthetic and field-based electrical imaging of zerovalent iron barrier: Implications for monitoring long-term barrier performance, *Geophysics*, *71*, 129–137.
Slater, L., W. Barrash, J. Montrey, and A. Binley (2014), Electrical-hydraulic relationships observed for unconsolidated sediments in the presence of a cobble framework, *Water Resour. Res.*, *50*, 5721–5742, doi:10.1002/2013WR014631.
Smith, M. J., J. Chandler, and J. Rose (2009), High spatial resolution data acquisition for the geosciences: Kite aerial photography, *Earth Surf. Processes Landforms*, *34*(1), 155–161.
Vereecken, H., A. Binley, G. Cassiani, A. Revil, and K. Titov (2006), *Applied Hydrogeophysics*, Springer, N. Y.
Titov, K., V. Komarov, V. Tarasov, and A. Levitski (2002), Theoretical and experimental study of time-domain-induced polarization in water saturated sands, *J. Appl. Geophys.*, *50*(4), 417–433.
Titov, K., A. Kemna, A. Tarasov, and H. Vereecken (2004), Induced polarization of unsaturated sands determined through time domain measurements, *Vadose Zone J.*, *3*, 1160–1168.
Triska, F. J., J. R. Sedell, K. Cromack Jr., S. V. Gregory, and F. M. McCorison (1984), Nitrogen budget for a small coniferous forest stream, *Ecol. Monogr.*, *54*(1), 119–140.
Vidon, P., C. Allan, D. Burns, T. P. Duval, N. Gurwick, S. Inamdar, R. Lowrance, J. Okay, D. Scott, and S. Sebestyen (2010), Hot spots and hot moments in riparian zones: Potential for improved water quality management, *J. Am. Water Resour. Assoc.*, *46*, 278–298, doi:10.1111/j.1752-1688.2010.00420.x.
Wainwright, H. M., J. Chen, D. S. Sassen, and S. S. Hubbard (2014), Bayesian hierachical approach and geophysical data sets for estimation of reactive facies over plume scales, *Water Resour. Res.*, *50*, 4564–4584, doi:10.1002/2013WR013842.
Wainwright, H. M., B. Dafflon, L. J. Smith, M. S. Hahn, J. B. Curtis, Y. Wu, C. Ulrich, J. E. Peterson, M. S. Torn, and S. S. Hubbard (2015), Identifying multiscale zonation and assessing the relative importance of polygon geomorphology on carbon fluxes in an Arctic tundra ecosystem, *J. Geophys. Res. Biogeosci.*, *120*, 788–808, doi:10.1002/2014JG002799.
Walling, D., D. Fang, A. P. Nicholas, R. J. Sweet, J. S. Rowan, R. W. Duck, and A. Werritty (2006), River flood plains as carbon sinks, in *Sediment Dynamics and the Hydromorphology of Fluvial Systems*, pp. 460–470, IAHS Publication, Oxfordshire OX10 8BB, U. K.
Weller, A., and D. L. Slater (2015), Induced polarization dependence on pore space geometry: Empirical observations and mechanistic predictions, *J. Appl. Geophys.*, *123*, 310–315, doi:10.1016/j.jappgeo.2015.09.002.
Wikle, C. K., R. F. Milliff, D. Nychka, and L. M. Berliner (2001), Spatiotemporal hierarchical Bayesian modeling: Tropical ocean surface winds, *J. Am. Stat. Assoc.*, *96*(454), 382–397.
Williams K.H., A. Kemna, M.J. Wilkins, J. Druhan, E. Arntzen, A. L. N'Guessan, P. E. Long, S. S. Hubbard and J. F. Banfield (2009), Geophysical monitoring of coupled microbial and geochemical processes during stimulated subsurface bioremediation, *Environ. Sci. Technol.*, *43*, 6717–6723.
Williams, K. H., et al. (2011), Acetate availability and its influence on sustainable bioremediation of uranium-contaminated groundwater, *Geomicrobiol. J.*, *28*(5-6), 519–539, doi:10.1080/01490451.2010.520074.
Wong, J. (1979), An electrochemical model of the induced polarization phenomenon in disseminated sulfide ores, *Geophysics*, *44*(7), 1245–1265.
Wrighton, K. C., et al. (2014), Metabolic interdependencies between phylogenetically novel fermenters and respiratory organisms in an unconfined aquifer, *ISME J.*, *8*(7), 1452–1463.
Yabusaki, S. B., Y. Fang, K. H. Williams, C. J. Murray, A. L. Ward, R. Dayvault, S. R. Waichler, D. R. Newcomer, F. A. Spane, and P. E. Long (2011), Variably saturated flow and multicomponent biogeochemical reactive transport modeling of a uranium bioremediation field experiment, *J. Contam. Hydrol.*, *126*(3-4), 271–290, doi:10.1016/j.jconhyd.2011.09.002.
Zachara, J. M., et al. (2013), Persistence of uranium groundwater plumes: Contrasting mechanisms at two DOE sites in the groundwater–river interaction zone, *J. Contam. Hydrol.*, *147*, 45–72.